Diploma Thesis DIPL-187

Reduced Model Design of a Floating Wind Turbine

by
Frank Sandner

Supervisors: Dipl.-Ing. D. Schlipf
Dipl.-Ing. D. Matha
Jun.–Prof. Dr.–Ing. R. Seifried

University of Stuttgart
ITM - Institute of Engineering
and Computational Mechanics
Prof. Dr.–Ing. Prof. E.h. P. Eberhard

SWE - Endowed Chair of Wind Energy at
IFB - Institute of Aircraft Design
Prof. Dr. Po Wen Cheng

July 2012

Contents

Acronyms and Abbreviations

AeroDyn	Aerodynamic module integrated in FAST
BEM	Blade Element Momentum Theory
CM	Center of mass
COB	Center of buoyancy
CPC	Collective Pitch Control
DEL	Damage Equivalent Load
DOF	Degree of freedom
IEC	International Electrotechnical Commission
EQM	Equation of motion
FAST	Fatigue, Aerodynamics, Structures and Turbulence (Simulation Tool by [1]
FFT	Fast Fourier Transform
FOWT	Floating offshore wind turbine
HAWT	Horizontal axis wind turbine
IFFT	Inverse Fast Fourier Transform
JONSWAP	Joint North Sea Wave Project
LIDAR	Laser wind speed measurement system (Light Detection And Ranging)
MBS	Multibody system
MSL	Mean sea-level
NEQ	Newton-Eulerian Equations
OC3	Offshore Code Comparison Collaboration, see [2]
ODE	Ordinary differential equation
PSD	Power Spectral Density
RAO	Response Amplitude Operator
SWL	Still water-level
WAMIT	Wave Analysis at MIT, marine engineering tool
WGN	White Gaussian Noise
WT	Wind turbine

Nomenclature

A_0	$[\mathrm{m}^2]$	Cross-sectional area of spar-buoy
$a_i^{isys}(z)$	$[\mathrm{m/s}^2]$	Platform acceleration in $i = 1, 2$-direction of *isys* at depth z
$a_{v/a}$	$[-]$	Constants for deepwater wave kinematics approximation, see section 3.4.1
$\boldsymbol{a}_i$	3×1	Total acceleration of body i
$\overline{\boldsymbol{a}}_i$	3×1	Local acceleration of body i
anchor		Anchor coordinate system (general description)
$b_{v/a}$	$[-]$	Constants for deepwater wave kinematics approximation, see section 3.4.1
$\boldsymbol{C}_{hydrostatic}$	6×6	Matrix of hydrostatic stiffness coefficients
C_A	$[-]$	Added-mass coefficient of Morison-equation (3.17)
C_D	$[-]$	Viscous drag coefficient of Morison-equation (3.17)
c	[m/s]	Wave propagation velocity or celerity
c_P	$[-]$	Power coefficient
c_T	$[-]$	Thrust coefficient
D	[m]	Spar-buoy diameter (also $D(z)$)
d_T	[Ns/m]	Tower damping constant
EA	[N]	Extensional stiffness of mooring lines, (2.30)
F_a	[N]	Thrust force on hub in shaft-direction
$\boldsymbol{F}_{aero}$	[N]	Aerodynamic force vector on rotor hub in *isys*
$\boldsymbol{F}_{hydro}$	[N]	Comprehensive hydrostatic and hydrodynamic forces on platform in *isys*
$\boldsymbol{F}_{Lines}$	[N]	Line force on fairleads in *anchor*-coordinate system
$\boldsymbol{F}_{mooring}$	[N]	Resulting mooring line forces at *frlds* in *isys*
$F_{mor,i}$	[N]	Horizontal hydrodynamic Morison Force ($i = 1, 2$)
$\boldsymbol{F}_{plant}$	[N]	Overall external forces on FOWT plant
$\boldsymbol{f}_i^e$	3×1	Vector of applied forces on body i

$\boldsymbol{f}_i^r$	3×1	Vector of reaction forces on body i
f		Number of degrees of freedom of MBS
frlds		Fairleads coordinate system
$\boldsymbol{g}$	$f \times 1$	Vector of reaction forces and torques, see (2.26)
g	$[\,\mathrm{m/s^2}]$	Acceleration constant
H	[m]	Significant wave height (trough to crest)
H_F	[N]	Horizontal line force on fairlead in line direction
h	[m]	Water depth
h_{tower}	[m]	Tower height from tower base to yaw bearing
$\boldsymbol{I}_i$	3×3	Mass moment of inertia of body i
isys		Inertial coordinate system
$\overline{\overline{\boldsymbol{J}}}$	$2 \cdot 3p \times f$	Global Jacobian matrix
$\boldsymbol{J}_{Ti}$	$3 \times f$	Translatory Jacobian matrix of body i
$\boldsymbol{J}_{Ri}$	$3 \times f$	Rotatory Jacobian matrix of body i
$\boldsymbol{k}$	$f \times 1$	Vector of generalized Coriolis-, centrifugal and gyroscopic forces, see (2.27)
k	[−]	Wavenumber
k_T	[N/m]	Tower stiffness constant
$\boldsymbol{l}_i^e$	3×1	Vector of applied torques on body i
$\boldsymbol{l}_i^r$	3×1	Vector of reaction torques on body i
L	[m]	Unstretched mooring line length
$L_{unstretched,x}$	[m]	Unstretched mooring line length projected on horizontal plane
l_{buoy}	[m]	Buoy length (bottom end to SWL in steady state)
$\overline{\overline{\boldsymbol{M}}}$	$2 \cdot 3p \times 2 \cdot 3p$	Global mass matrix, see (2.27)
$\boldsymbol{M}$	$f \times f$	Mass matrix of NEQ
M_{aero}	[Nm]	Aerodynamic torque on the rotor about shaft
$M_{F,y}$	[Nm]	Torque from lines on fairleads about $isys_2$-axis
M_g	[Nm]	Generator torque about shaft (> 0)
$M_{wtrplnarea}$	[Nm]	Hydrostatic moment on structure from waterplane area
$\boldsymbol{m_i}$	3×3	Mass matrix of body i
nacelle		Local nacelle coordinate system
$\boldsymbol{p}$	$f \times 1$	Vector of generalized forces, see (2.27)
P_{tower}	[−]	Normalized polynomial describing the first tower eigenmode, see (2.7)
ptfm		Local platform coordinate system
*ptfm**		Coordinate system with origin at *ptfm* and a constant orientation of *isys*, see (3.17)
p		Number of bodies of MBS
$\overline{\overline{\boldsymbol{Q}}}$	$2 \cdot 3p \times f$	Distribution matrix, see (2.26)
$\boldsymbol{q}$	$f \times 1$	Vector of degrees of freedom

$\boldsymbol{q}_{ptfm,SWL}$	$f \times 1$	Platform degrees of freedom defined at SWL
$\overline{\boldsymbol{q}}^c$	$2 \cdot 3p \times 1$	Vector of Coriolis-, centrifugal and gyroscopic forces, see (2.26)
$\overline{\boldsymbol{q}}^e$	$2 \cdot 3p \times 1$	Vector of applied forces (e.g. gravitational, spring), see (2.26)
$\boldsymbol{r}_i$	3×1	Position vector of body i
$\dot{\boldsymbol{r}}_i$	3×1	Derivative of position vector of body i relative to *isys*
$\boldsymbol{r}_z^{ptfm}$	3×1	Position vector to a platform strip at depth z in *ptfm*-coordinates
R	[m]	Rotor radius
rotor		Local rotor coordinate system with origin at CM
$\boldsymbol{S}$	3×3	Rotation tensor
S_η^{1sdd}	$\mathrm{rad}^2/\mathrm{s}^2/\mathrm{Hz}$	One-sided wave amplitude spectrum
S_η^{2sdd}	$\mathrm{rad}^2/\mathrm{s}^2/\mathrm{Hz}$	Two-sided wave amplitude spectrum
swl		Platform-fixed coordinate system at SWL
tower		Local tower coordinate system
$\boldsymbol{v}_i$	3×1	Total velocity of body i
$\hat{v}$	[m/s]	Amplitude of fluid velocity normal to structure
$v_i^{isys}(z)$		Platform velocity in $i = 1, 2$-direction of *isys* at depth z
V_F	[N]	Vertical line force on fairlead in line direction
v_0	[m/s]	Scalar wind speed after reducing vector field over the rotor plane
$v_{rel,shft}$	[m/s]	Rotor-effective wind speed in shaft-direction
v_{rel}	[m/s]	Rotor-effective wind speed in horizontal direction
$W(\omega)$	[−]	Fourier-transform of white gaussian noise with unit variance (through Box-Muller Method)
x_F	[m]	Horizontal fairleads displacement from initial position in line-direction
$\boldsymbol{x}$	$2f \times 1$	State vector
wave		Wave coordinate system, equals *isys* but points in wind direction
z_0	[m]	Vertical distance from SWL to COB
z_{buoy}	[m]	Vertical distance from SWL to bottom end of buoy
z_{CM}	[m]	Vertical distance from SWL to platform center of mass
z_{COB}	[m]	Vertical distance from SWL to platform center of buoyancy
z_F	[m]	Vertical fairleads displacement from initial position in line direction

α	[deg]	Rotation angle about first axis applying $\boldsymbol{S}$, see (2.15)
β	[deg]	Rotation angle about second axis applying $\boldsymbol{S}$, see (2.15)
β_i	[deg]	$i = 1 \ldots 3$ Horizontal mooring line direction towards $isys_1$-axis
γ	[deg]	Rotation angle about third axis applying $\boldsymbol{S}$, see (2.15)
ζ		First coordinate normal to buoy axis for volume integral (3.4)
η	[m]	Free surface wave elevation from SWL (linear waves)
θ	[deg]	Blade pitch angle
λ	[m]	Wave length (chapter 3)
λ	[−]	Tip-speed ratio (chapter 4)
ξ		Second coordinate normal to buoy axis for volume integral (3.4)
ϕ	3×1	Velocity potential (Potential flow theory)
ρ	[kg/ m^3]	Fluid density
φ	[deg]	Tilt angle (about $tower_2$-axis)
ψ	[deg]	General formulation of buoy angle towards vertical axis
Ω	[rad/s]	Rotor angular velocity
ω	[rad/ s]	Wave frequency
ω	[N/m]	Equivalent mooring line weight in water
$\boldsymbol{\omega}_i$	3×1	Angular velocity of body i
$\tilde{\boldsymbol{\omega}}_i$	3×1	Skew-symmetric matrix corresponding to $\boldsymbol{\omega}_i$

Abstract

Floating platform concepts offer the prospect of harvesting offshore wind energy at deep water locations for countries with a limited number of suitable shallow water locations for bottom-mounted offshore wind turbines. The floating spar-buoy concept has shown promising experimental and theoretical results. Although various codes for a detailed simulation exist the purpose of this work is to elaborate a reduced Floating Offshore Wind Turbine (FOWT) model that mainly reproduces the overall nonlinear low-frequency behaviour of the system with a significant saving in simulation time. One objective is to extend the model predictive control algorithm that has previously been developed for onshore wind turbines to the FOWT for motion control and load reductions. Another objective is a fast dynamic assessment of new concepts during design phase with respect to load cases defined by the International Electrotechnical Commission (IEC).
The platform and wind turbine structure is modelled as a three-dimensional multibody system consisting of four rigid bodies with nine degrees of freedom. That is, unconstrained platform motion, tower bending in two directions and variable rotor speed. The coupled nonlinear system of equations of motion is calculated symbolically using the Newton-Euler formalism that takes Coriolis- and centrifugal forces into account. Complex disturbances on the system arising from aerodynamics and hydrodynamics are simplified along with the model as efficiently and accurately as possible. Wind loads are predicted by reducing the three-dimensional turbulent wind field to a scalar rotor-effective wind speed also considering restoring torques resulting from oblique inflow. Linear wave theory provides the wave kinematics and wave loads are calculated using the relative formulation of Morison's Equation. An approach is presented to estimate wave loads on the floating structure based only on real-time wave height measurements. This allows also for an analytical calculation of wave loads in time-domain without iterative or recursive algorithms so that a significant saving in computational time is achieved. The presented disturbance reduction to simple and measurable inputs for wind and waves is a precondition for the implementation of an optimal control algorithm. The reduced nonlinear model is compared to the certified aero-hydro-servo-elastic FAST model in time and frequency domain. The results are promising as there is good agreement in static and dynamic response.

Chapter 1

Introduction

Why is it necessary to build offshore wind turbines that are not fixed to the seabed but merely float on the water surface? Global energy consumption was 152 TWh in 2011[1]. Only a share of sixteen percent of this value is produced by hydroelectricity, the major renewable energy source. Generating electric power out of kinetic and potential energy of water is the renewable energy source that has been applied from the beginning of electric energy production. It stands out amongst other renewable energy sources through its non-volatility. Although wind power has been traditionally used far before electricity and its worldwide potential ranges second following solar power [3] its universalized use is confronted by diverse obstacles. Whereas onshore wind power has become a highly reliable and in industrialized countries prevalent renewable energy source economically suitable locations are limited. In order to cope with global transitions like the increasing population and energy demand more sophisticated systems of harnessing energy have to be established and capital intensive technologies accepted. In terms of wind power this means extending the application of offshore wind turbines to countries with deeper seas. Along with this development engineering challenges arise through very hostile environmental conditions but at the same time one can take advantage of higher average wind speeds with less variation. A total power of 27.000 MW is produced by offshore wind in Germany by 2011 [4]. Although the installation costs for offshore plants exceed those onshore the larger scale of used turbines helps to lower energy generation costs down to 6 ct/kWh [5], which makes it even competitive to fossil fuels not considering the various environmental externalities. The average water depth at offshore wind park locations was 17.4 m in 2010 and has increased to 22.8 m in 2011. The distance to the coast shows the same trend with an average of about 25 km. Wind park "Bard Offshore 1" is located at a distance of 90 km to the isle of Borkum at a water depth of 40 m [6].

[1] Enerdata, Grenoble/France: Total energy consumption 2011. Accessed 23/07/12.

The majority of foundation architectures is a monopile which is rammed into the seabed [6]. However, this method is limited to a depth of 30 m and is criticized because of high noise levels during construction that impact marine fauna. For depths up to 10 m the gravity-based foundation is an alternative without penetration of the seabed. Jacket constructions are adopted from oil and gas industry and are applied in 20 % of the 2011 installed offshore wind turbines (WT). They are suitable for deeper water depths and save material compared to monopiles. A comparable structure is the tripod that is applied in 10 % of offshore WT installations of 2011. However, the economical depth-limit for bottom mounted applications is 60 m. This fact illustrates the necessity of making offshore wind power more flexible to other locations. While the distance to the coast is limited by cost-intensive sea cables the methods of mounting wind turbine towers are manifold and therefore the extension to countries with a steeper coastal topography is possible.

The method of building stationary offshore structures without fixing them rigidly to the ground is known from oil and gas industry. Up to 2012 various concepts for floating offshore wind turbines (FOWT) have been elaborated and technically as well as economically assessed like in [7]. The concepts differ in their way of ensuring a restoring moment on the floating body which is the most relevant characteristic. Stabilizing restoring can have its origin in the amount of submerged volume relative to angular displacement ("waterplane area"), the location of the center of buoyancy with respect to the center of mass ("metacentric height") or the system of mooring lines going down to the seabed. Three full-scale prototypes for floating offshore wind turbines have been built so far, among them the "Hywind" spar-buoy which serves as a reference in this work. A spar-buoy is a cylindrical structure which floats vertically allowing a very low location of the center of gravity and thus a large metacentric height as the hollow geometry is filled with ballast chipping to a certain level. Catenary mooring lines ensure station-keeping. This concept features a high natural stability without any form of active control. Other concepts, like the "WindFloat" project, rely more on waterplane area avoiding a long draft so that shallower coasts are also applicable for the floater concept. In this concept a semi-submersible structure consisting of three tubular bodies that are mutually connected with the same form of catenary moorings serves as foundation. A third common method for floating foundations is the tension leg platform (TLP). Here a mostly flat buoyant body is pulled under water by taut mooring lines in a way that incident wave forces are always smaller than the stabilizing line forces. All methods aim at a stable foundation that is not excessively impacted by incident waves or extreme gusts of wind. As wave-induced forces are strongest

close to the water surface ways are sought to circumvent a big structural surface around mean sea level (MSL). A concept featuring a body that is only slightly submerged and therefore mainly floating on the water surface is the buoyancy stabilized barge concept with catenary mooring lines. Up to 2012 only one of these concepts, is grid-connected. Challenges are extreme-incidence loads which have to be taken into account during design, rising the costs and also a reliable life time prediction. Research also aims at systemic grid optimization taking energy transportation and storage into account. Therefore coupled concepts are being considered which combine a wave energy converter with wind turbines mounted on the same floating body.

The motivation of this work is to elaborate a simplified model of the whole floating wind turbine plant that reliably represents the overall nonlinear low-frequency behaviour. A related project has been carried out at NTNU, Norway, see [8]. That approach is also focused on simplicity and speed but applies other methodologies with respect to the structural dynamic model and aims at different applications. One objective is to apply the code as internal model of a controller in order to extend Nonlinear Model Predictive Control (NMPC) for the spar-buoy floating offshore concept. Modern wind turbines operate at fixed or variable rotor angular speed with variable pitch angle of the blades. While a torque controller ensures an optimal angular speed of the rotor the pitch controller limits the produced power around and above rated wind speed. Numerous closed-loop control strategies have been elaborated mostly pursuing the goal of optimal energy harnessing and load reduction given a certain wind speed. With NMPC multiple optimization targets are possible, for example a reduction of Damage Equivalent Loads (DEL) or the least possible actuator activity. Given the simple design of the spar-buoy and its advantages in terms of reliability no new actuators are added but the pitch control extended instead. In order to allow for a reduction of extreme loads coming from waves or wind gusts advanced sensors are used. With LIDAR (Light Detection and Ranging) wind speeds ahead of the turbine can be measured allowing optimal control within a certain time frame, see [9]. Measurements of wave height (e.g. using buoys) also allow to predict wave loads on the structure. Eventually a realistic mathematical model of the whole plant is needed so that the controller accesses sensor data that is input as disturbance to the internal dynamic model. Therewith an optimal control algorithm yields the most stable and efficient operation of the FOWT.
Besides the application of the reduced model within model predictive control one can take advantage of the low computational effort and apply the code for the numerous load case simulations that are necessary during design phase of new concepts, see [10].

This work is organized as to first introduce all components preparing for the

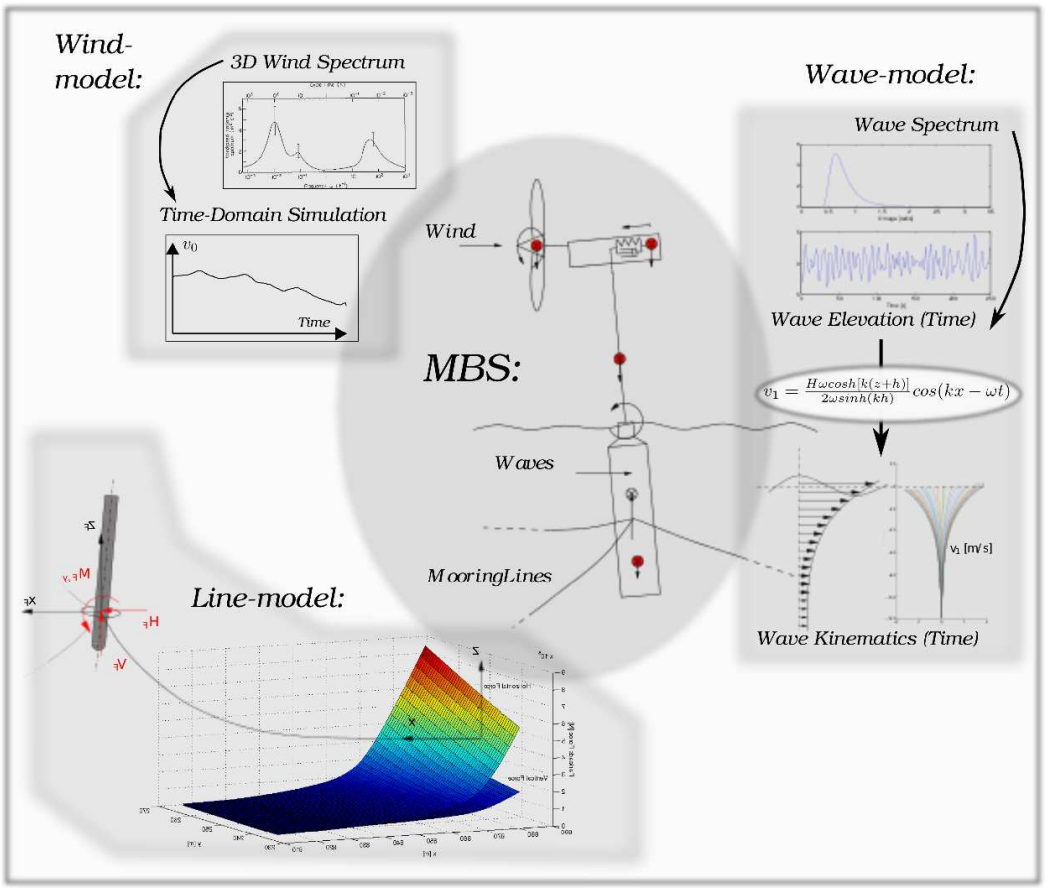

Figure 1.1: Floating wind turbine model.

realization of the overall dynamic model. The set-up of a FOWT-numerical model can be divided into several subsystems consisting of the central structural model that interacts with the mooring system and is impacted by the external forces from wind and waves. Thus, the subsystem for aerodynamic loads and the one for hydrodynamic loads complete the coupled FOWT model, see figure 1.1. At the beginning of each chapter the conventional modelling strategies are shortly addressed before the reduced approach is presented and discussed. Chapter 2 gives details on the multibody model of the whole floating structure. The external forces being applied on that model coming from hydrodynamics are the focus of chapter 3 followed by chapter 4 which explains the employed aerodynamic model. Chapter 5 gives a short description of how the dynamic simulation is performed with pre- and post-processing. All features of the code and available options are presented. With the model evaluation comparing dynamic responses to the full aero-hydro-servo-elastic model in chapter 6 the work is finalized and conclusions and an outlook for further work is given in chapter 7.

Chapter 2

Floating Offshore Wind Turbine Structural Model

The structural model is the central part of the overall numerical FOWT model. Its coupled equations of motion include all external forces that are calculated in separate subsystems. Many sophisticated structural models exist that divide the plant into small separate bodies that are dynamically linked with each other. Flexible multibody systems (MBS) allow the description of bodies and associated degrees of freedom (DOF) that account for body deformation. Numerical reduction methods are then applied in order to reduce the high order of ordinary differential equations (ODE) still reproducing the model characteristics that are to be considered. The reference model FAST, see [1], simulates a system of 22 dofs with the three turbine blades and the tower modelled as flexible bodies representing dynamics up to the second mode in two directions as well as variable rotor-speed.

For the reduced model a rigid multibody system approach is chosen. The system consists of four rigid bodies with an associated lumped inertial mass and a mass moment of inertia. The only elastic part is a spring-damper element representing tower deformation whereas the remaining bodies platform, nacelle and rotor are fully indeformable. The rotor is represented by a disk-like body attributed with a mass and a mass moment of inertia without any degrees of freedom allowing bending of the blades. These simplifications are, however, reasonable since the structure is dominated by rigid body motions and major dynamic excitations on the FOWT range from wave loads of about 0.1 Hz to rotor-induced oscillations of 0.2 Hz. High aerodynamic damping mostly dissipates high-frequency blade oscillations so that the frequency spectrum of onshore-WT shows a characteristic cut-off frequency of 0.2 Hz, see [9]. A total set of nine degrees of freedom allows three-dimensional translatory and rotational motion of the platform, tower

bending and a variable rotor speed.

The mathematical model has been elaborated using the Newton-Euler formalism which takes all dynamic effects of local rotations like Coriolis and gyroscopic forces into account, see [11]. This is possible through the momentum and angular momentum equations of each body that are combined in a coupled system of ODEs. A symbolic derivation of the set of equations allows for simple adding and removing of bodies or degrees of freedom. A sketch of the mechanical model indicating the bodies and their degrees of freedom as well as coupling elements and external forces is given in figure 2.1, where all external forces are input into the MBS with *isys*-orientation. The used geometric data can be found in the sketch A.1 in the appendix. All employed gravitational and inertial mass data is taken from the OC3-Code Comparison Collaboration, see [2].

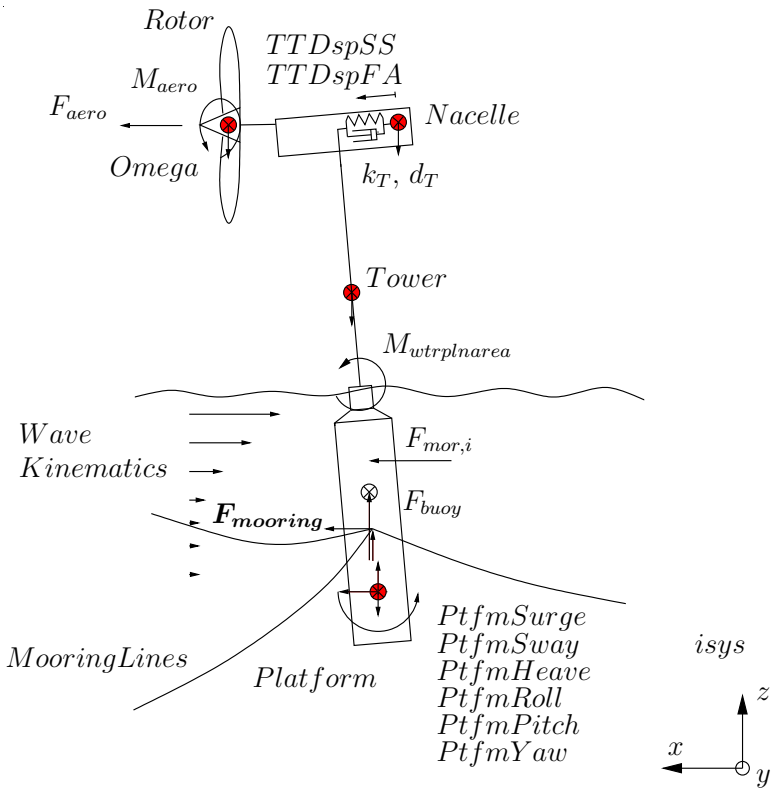

Figure 2.1: Floating wind turbine mechanical model.

The equations of motion of the floating wind turbine are derived in the following starting with the kinematics in section 2.1.1. These are followed by the kinetics in section 2.1.2 so that the whole set of equations is put together in section 2.1.3. The model of the mooring system is topic of the last section of chapter 2.2.

2.1 Reduced model structural dynamics

In order to derive the equations of motion of the reduced 3D multibody system the coupled momentum and angular momentum equations are set up. The $p = 4$ rigid bodies, *Platform, Tower, Nacelle* and *Rotor* have $f = 9$ degrees of freedom, allowing plant motion in x-, y- and z-direction of the inertial coordinate system.

2.1.1 Floating wind turbine kinematics

The generalized coordinates describing the degrees of freedom are

$$\boldsymbol{q} = \begin{bmatrix} PtfmSurge \\ PtfmSway \\ PtfmHeave \\ PtfmRoll \\ PtfmPitch \\ PtfmYaw \\ TTDspFA \\ TTDspSS \\ Omega \end{bmatrix} \tag{2.1}$$

giving the displacement vector $\boldsymbol{q}$. The first six entries are the platform translatory and rotational degrees of freedom at the platform center of mass. All translatory degrees of freedom are defined in the inertial frame of reference $isys$. Rotational degrees of freedom depend on the sequence of rotation of the platform body that is further described in section 2.1.1. The seventh and eighth entry is the tower fore-aft and side-side motion caused by tower bending. Both are defined as being translatory only in the platform coordinate system since the deflections are small and a translatory rather than a rotational description is more convenient. The last degree of freedom is the one allowing the rotor to rotate. *Omega* indicates the angle and not the angular speed. As the rotor is modelled as a disk that is attributed only with a mass and a moment of inertia the angle *Omega* is in fact not a state as the velocity suffices to describe the equations of motion. However, it is included here for reasons of consistency.

In a first step, the p position vectors $\boldsymbol{r}_i$ in the inertial reference frame *isys* depending on the degrees of freedom are defined. Using rotation tensors $\boldsymbol{S}_i$ for each body makes it easy to first set up a local vector and transforming it subsequently. The position vector of each body's center of mass is set up. For the position of

the platform remains with the constant $c_{1,z}$

$$\boldsymbol{r}_{ptfm}^{isys} = \begin{bmatrix} q_1 \\ q_2 \\ c_{1,z} + q_3 \end{bmatrix}. \tag{2.2}$$

Geometrical constants as well as degrees of freedom determine each body's position. The angular speed of each body completes the explicit description of the position in space. For the platform and equally for the tower and nacelle remains

$$\boldsymbol{\omega}_{ptfm}^{isys} = \boldsymbol{S}_{roll} \cdot \begin{bmatrix} \dot{q}_4 \\ 0 \\ 0 \end{bmatrix} + \boldsymbol{S}_{roll} \cdot \boldsymbol{S}_{yaw} \cdot \begin{bmatrix} 0 \\ 0 \\ \dot{q}_6 \end{bmatrix} + \boldsymbol{S}_{roll} \cdot \boldsymbol{S}_{yaw} \cdot \boldsymbol{S}_{pitch} \cdot \begin{bmatrix} 0 \\ \dot{q}_5 \\ 0 \end{bmatrix}. \tag{2.3}$$

Please see the end of this section for a further description of rotations. Coordinate systems *frlds, swl, nacelle* and *tower* rotate with the same angular speed as the platform. The coordinate system at the rotor center of mass, however, includes further rotations about y. Eventually the rotation tensor of the rotor takes the form

$$\boldsymbol{\omega}_{rotor}^{isys} = \boldsymbol{\omega}_{ptfm}^{isys} + \boldsymbol{S}_{rotor} \cdot \begin{bmatrix} \dot{q}_9 \\ 0 \\ 0 \end{bmatrix} \tag{2.4}$$

with

$$\boldsymbol{S}_{rotor} = \boldsymbol{S}_{roll} \cdot \boldsymbol{S}_{yaw} \cdot \begin{bmatrix} \cos(\varphi_{rotor}) & 0 & \sin(\varphi_{rotor}) \\ 0 & 1 & 0 \\ -\sin(\varphi_{rotor}) & 0 & \cos(\varphi_{rotor}) \end{bmatrix}. \tag{2.5}$$

where φ_{rotor} is given by

$$\varphi_{rotor} = q_5 + \varphi_{shaft} + \varphi_{twrbend}. \tag{2.6}$$

Thus, the rotor coordinate system is additionally tilted relative to the platform coordinate system by the commonly designed shaft-tilt angle φ_{shaft}. The second angle about the y-axis, $\varphi_{twrbend}$, represents the inclination of the nacelle induced by tower bending. The tower is modelled as a spring-damper element representing the first bending mode only with the translatory tower top fore-aft degree of freedom q_7 in *tower*-coordinates. Thus, the rotation at tower top going along with tower bending needs to be modelled. Therefore Bernoulli's Beam Theory is applied. It makes the assumption that all cross-sectional areas of a bent beam-like structure remain perpendicular to the neutral fibre. The angle $\varphi_{twrbend}$ is here calculated using the normalized polynomial description of the first modal shape of the tower P_{tower}, given in [12] and will take the form

$$\varphi_{twrbend} = arctan(\frac{dP_{tower}}{dz}\frac{\boldsymbol{q}_7}{h_{tower}}). \tag{2.7}$$

It is assumed that side-side deflections at tower top are small compared to the fore-aft deflections. This is why nacelle inclination is only approximated about the y-axis. The effect of tower top inclination on the system is mostly determined by the aerodynamic forces that depend on the orientation of the rotor towards wind speed, see chapter 4.
The eventual goal is to set up the spatial momentum and angular momentum equations for each body where the center of gravity is used as reference point. Therefore the corresponding translatory and rotational accelerations for each body must be computed. Jacobi-matrices $\boldsymbol{J}_{Ti}$ and $\boldsymbol{J}_{Ri}$ allow to separate curvilinear motions into different translatory and rotational directions of the inertial coordinate system. The translatory velocity is given by

$$\boldsymbol{J}_{Ti} = \frac{\partial \boldsymbol{r}_i}{\partial \boldsymbol{q}} + \bar{\boldsymbol{v}}_i \tag{2.8}$$

and

$$\bar{\boldsymbol{v}}_i = \frac{\partial \boldsymbol{r}}{\partial t}. \tag{2.9}$$

Rotational Jacobi-matrices are conveniently found from the relation

$$\boldsymbol{\omega}_i = \boldsymbol{J}_{Ri}(\boldsymbol{q}) \cdot \dot{\boldsymbol{q}} + \bar{\boldsymbol{\omega}}_i. \tag{2.10}$$

The local velocities $\bar{\boldsymbol{v}}_i$ and angular velocities $\bar{\boldsymbol{\omega}}_i$ vanish in scleronomic systems as the one considered here. In order to complete the kinematics to formulate the momentum equations the generalized accelerations have to be calculated by differentiating the position vectors twice. The vectorial absolute differentiation of the curvilinear motions specified by $\boldsymbol{q}$ and $\boldsymbol{J}_{Ti}$ appears in algebraic formulation with the total time derivative of each body's Jacobian-matrix

$$\dot{\boldsymbol{J}}_{Ti} = \frac{d}{dt}\frac{\partial \boldsymbol{r}_i}{\partial \boldsymbol{q}} \tag{2.11}$$

as

$$\boldsymbol{a}_i = \dot{\boldsymbol{v}}_i = \boldsymbol{J}_{Ti} \cdot \ddot{\boldsymbol{q}} + \dot{\boldsymbol{J}}_{Ti} \cdot \dot{\boldsymbol{q}}. \tag{2.12}$$

The angular accelerations can be calculated in a similar way as

$$\boldsymbol{\alpha}_i = \dot{\boldsymbol{\omega}}_i = \boldsymbol{J}_{Ri} \cdot \ddot{\boldsymbol{q}} + \dot{\boldsymbol{J}}_{Ri} \cdot \dot{\boldsymbol{q}}. \tag{2.13}$$

For a further understanding of the plant dynamics equation (2.12) is rewritten in a geometrically more ostensible way with the local position vector $\boldsymbol{r}_i^{isys}$

$$\boldsymbol{a}_i = \underbrace{\boldsymbol{a}_{ptfm}}_{translational} + \underbrace{\frac{d}{dt}\boldsymbol{\omega}_{ptfm} \times \boldsymbol{r}_i^{isys}}_{tangential} + \underbrace{\boldsymbol{\omega}_{ptfm} \times (\boldsymbol{\omega}_{ptfm} \times \boldsymbol{r}_i^{isys})}_{centripetal} + \underbrace{2\boldsymbol{\omega}_{ptfm} \times \boldsymbol{v}_{i,rel}}_{Coriolis} \tag{2.14}$$

Vector $\boldsymbol{r}_i^{isys}$ stands for coordinate systems which rotate with the platform like the tower, see figure 2.2. The first two terms of the right hand side of equation (2.14) equal the term ($\boldsymbol{J}_{Ti}\ddot{\boldsymbol{q}}$) of equation (2.12). The first term itself is translational only, the second is tangential to a curvature, whereas the centripetal contribution to total acceleration points towards the center of the curvature. The last term, the Coriolis acceleration also points towards the center of the curvature but is induced by translatory velocities in a rotating frame of reference. Relative accelerations do not appear in this model and are therefore neglected in equation (2.14). The last part of this section on kinematics will give more details on the description of rotations of the reduced model.

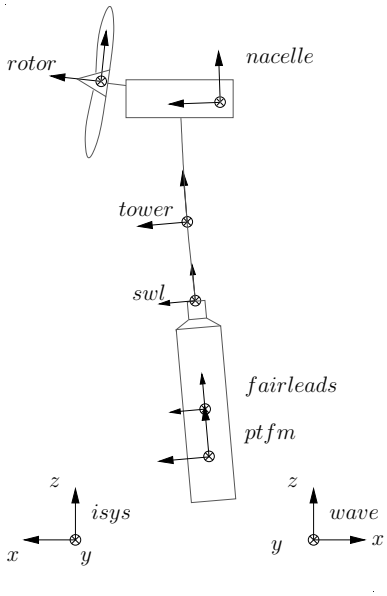

Figure 2.2: FOWT kinematics.

Rotation tensors

The three-dimensional rotation of the FOWT platform requires an adequate mathematical description. A principal difference to two-dimensional rotations is that specific axes of rotation have to be determined. Many formulations include an axis of rotation that remains constant either for an infinitesimal rotation or for one sequential step of rotation. Quaternions consist of four coordinates and one constraint, so that one coordinate describes the angle and the remaining three give the axis of rotation. Euler and Kardan angles are defined as a sequence of rotations about the axes of the transformed coordinate system itself. This implies that the axes of rotation are not perpendicular to each other and not the axes of a single coordinate system but the ones resulting from each sequential

step of rotation. Therefore, the sequence of rotation or the sequence of rotation matrices applied on a vector is not commutative. For small angles the rotation sequence can be neglected as is done in the reference code FAST, see [12]. Here, a way is sought to implement a description of plant rotations that is most suitable for the specific model. Looking at the floating wind turbine it is apparent that little torques arise about the x-, and z-axes but a non-negligible torque about the y-axis appears resulting from the thrust force on the rotor. Out of this reason the sequence of rotations is chosen as to rotate first about x (α), then about z (γ) and lastly about y (β). Consequently, the description is closely related to a sequential rotation about the axes of the inertial coordinate system. This feature is also important for the linearization of kinematics, described later in this section. Eventually the rotation matrix $\boldsymbol{S}$ takes the form

$$\boldsymbol{S} = \begin{bmatrix} 1 & 0 & 0 \\ 0 & \cos(\alpha) & -\sin(\alpha) \\ 0 & \sin(\alpha) & \cos(\alpha) \end{bmatrix} \cdot \begin{bmatrix} \cos(\gamma) & -\sin(\gamma) & 0 \\ \sin(\gamma) & \cos(\gamma) & 0 \\ 0 & 0 & 1 \end{bmatrix} \cdot \begin{bmatrix} \cos(\beta) & 0 & \sin(\beta) \\ 0 & 1 & 0 \\ -\sin(\beta) & 0 & \cos(\beta) \end{bmatrix} \tag{2.15}$$

resulting in

$$\boldsymbol{S} = \begin{bmatrix} \mathrm{c}_\gamma \mathrm{c}_\beta & -\mathrm{s}_\gamma & \mathrm{c}_\gamma \mathrm{s}_\beta \\ \mathrm{s}_\alpha \mathrm{s}_\beta + \mathrm{c}_\alpha \mathrm{c}_\beta \mathrm{s}_\gamma & \mathrm{c}_\gamma \mathrm{c}_\alpha & \mathrm{c}_\alpha \mathrm{s}_\gamma \mathrm{s}_\beta - \mathrm{c}_\beta \mathrm{s}_\alpha \\ \mathrm{c}_\beta \mathrm{s}_\gamma \mathrm{s}_\alpha - \mathrm{c}_\alpha \mathrm{s}_\beta & \mathrm{c}_\gamma \mathrm{s}_\alpha & \mathrm{c}_\alpha \mathrm{s}_\beta + \mathrm{s}_\gamma \mathrm{s}_\alpha \mathrm{s}_\beta \end{bmatrix} \tag{2.16}$$

where the trigonometric functions $\sin(x)$ and $\cos(x)$ are abbreviated with s_x and c_x. Rotations in space can lead to very large equations of motion. This can result in high computational effort which is sought to be reduced for this model. A possible measure to this is to linearize kinematics and to linearize rotation tensors.

Rotation tensors are the only source of trigonometric functions to the equations of motion. As a consequence, further linearization of quantities other than the rotation tensors will only concern coupled and quadratic terms if the linearization results in first-order terms only. An important geometric feature of the FOWT is, however, the plant height which means that small rotations about the platform center of mass will result in large displacements of the nacelle. Thus, linearization of the description of rotation is only valid in a narrow range around the operating point. Another difficulty is that the rotation tensors loose their orthogonality when being linearized. The simulation tool FAST uses an alternate rotation tensor that avoids trigonometric functions, see [12]. All simulations of this model are performed with fully nonlinear rotation tensors. It is to be further determined in which range linearized kinematics influence dynamic results.

2.1.2 Floating wind turbine kinetics

External forces on the plant are the gravitational forces being exerted on each body's center of mass, the aerodynamic forces, hydrostatic and hydrodynamic forces, wave excitation forces and the ones resulting from the mooring system

$$\boldsymbol{F}_{plant} = \sum_{i=1}^{n} m_i g + \boldsymbol{F}_{mooring} + \boldsymbol{F}_{hydro} + \boldsymbol{F}_{aero}, \tag{2.17}$$

see also figure 2.1 for an illustration. External torques are coming from the hydrostatic restoring torque $M_{wtrplnarea}$ which is further described in section 3.1. Other than that aerodynamic lift forces on the blades result in a torque about shaft axis which yields a small angular platform yaw displacement in steady state because the shaft is mostly tilted about y so that this torque contains a portion about the z-axis. More details about aerodynamic forces and torques are presented in chapter 4. Mooring forces $\boldsymbol{F}_{mooring}$ and the lines model are described in section 2.2. Hydrostatic and hydrodynamic forces $\boldsymbol{F}_{hydro}$ which are applied on the platform are described in detail in chapter 3. As various hydrostatic and hydrodynamic constants are calculated by external tools and returned at mean sea level (MSL) a torque about the platform center of mass arises for each of these forces. In the same way torques on the platform result from mooring forces as the fairleads coordinate system does not coincide with the platform center of mass, see figure 2.2. The vectorial calculation of these moments takes the form

$$\boldsymbol{T}_k = (\boldsymbol{S}_{ptfm}^{isys} \cdot \boldsymbol{r}_k^{ptfm}) \times \boldsymbol{F}_k \tag{2.18}$$

with the local vector $\boldsymbol{r}_k^{ptfm}$ pointing to the location where force $\boldsymbol{F}_k$ is applied. Aerodynamic forces $\boldsymbol{F}_{aero}$ are applied on the rotor, only. Their origin is further derived in chapter 4.

Internal forces appear at the interfaces of coupling elements. The reduced FOWT model features one dynamic link between nacelle and tower. This adds the translational degree of freedom of tower top fore-aft (*TTDspFA*) and side-side (*TTDspSS*) displacement. The dynamic coupling is characterized by the mass distribution of both bodies connected to the spring-damper and its stiffness and damping constants. Since the tower itself is now regarded as coupling element its mass has to be distributed. According to [13] the tower mass is split up attributing 25 % to the nacelle and the remaining part to the tower body itself. This assumption is taken as a basis for the determination of spring and damping coefficients. A step response simulated with the reference model FAST [1] gives the free decay information. With the equation for the harmonic oscillator

$$\ddot{x} = 2D\omega_0\dot{x} + \omega_0^2 x = \frac{d}{m}\dot{x} + \frac{k}{m}x \tag{2.19}$$

the damping constant d can be calculated based on the experimentally determined damping ratio D. This results from the logarithmic decay that is depicted in figure 2.3 with two consecutive amplitudes

$$\Lambda = \ln\left(\frac{\hat{x}_i}{\hat{x}_{i+1}}\right) \tag{2.20}$$

and it follows

$$D = \sqrt{\frac{1}{1+\frac{4\pi^2}{\Lambda^2}}}. \tag{2.21}$$

With this information the undamped natural frequency ω_0 can be calculated which on the other hand allows the determination of the spring constant k, see equation (2.19). The resulting parameters of tower kinetics are summarized in

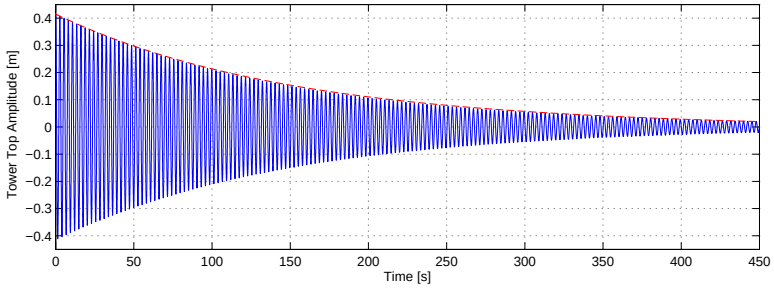

Figure 2.3: Tower Free Decay.

table 2.1. Apart from the force magnitudes that are found with k_T and d_T it is now necessary to take a further look at the direction of the exerted force. The spring-damper element related to the *TTDspFA*-DOF connects the nacelle center of mass with the tower body in perpendicular direction to the tower centerline, see figure 2.1. The *TTDspSS*-DOF on the other hand does not connect to the nacelle center of mass but right to the point where the nacelle is coupled with the tower on its centerline. Consequently, a resulting torque has to be included in the torque vector of the nacelle $l^e_{nacelle}$ with the distance between tower centerline and nacelle center of mass $NacxDW$ as lever arm, see figure A.1 in the appendix. Apart from the tower-nacelle coupling that is now identified the tower inertia is not directly given in [2] so that the value has been numerically calculated based on geometry data in the same way as for the rotor. Please also find the according values in Table 2.1.
As last part of this section the link between generator and nacelle is considered. The aerodynamic torque M_{aero} acts externally on the rotor but it is eventually backed by the generator which produces the reaction-torque. Thus, the rotor body actually experiences the resultant torque $M_g - M_{aero}$. As a consequence, the nacelle is impacted by the external torque M_g about the shaft axis.

At this point all necessary terms for formulating the vectorial momentum equation in absolute coordinates are given. The next section finalizes the formulation of the set of equations of motion.

Table 2.1: Additionally identified model data.

Tower stiffness	$k_T =$	$5.65872 \cdot 10^3$	N/m
Tower damping	$d_T =$	$2.2463 \cdot 10^6$	Ns/m
Total tower mass	$m_T =$	$2.4972 \cdot 10^5$	kg
Tower inertia about y and z	$I_{T,yy} = I_{T,xx} =$	$2.6763 \cdot 10^9$	kgm^2
Rotor Inertia about y and z	$I_{R,yy} = I_{R,xx} =$	$1.7664 \cdot 10^7$	kgm^2
Off-diagonal rotor inertia	$I_{R,yz} =$	$-1.0198 \cdot 10^7$	kgm^2

2.1.3 Newton-Euler Equations

With the described kinetics the equations of motions can be written. The first set of equations, equation (2.22), represents Newton's second law, meaning that the momentum equation is set up for each body in each spatial direction. The second set, equation (2.23), represents the angular momentum equations for each body. Newtons second law remains for each body in direction i as

$$\boldsymbol{m}_i \cdot \boldsymbol{a}_i = \boldsymbol{m}_i \cdot \boldsymbol{J}_{Ti} \cdot \ddot{\boldsymbol{q}} + \boldsymbol{m}_i \cdot \overline{\boldsymbol{a}}_i = \boldsymbol{f}_i^e + \boldsymbol{f}_i^r. \tag{2.22}$$

The term $\overline{\boldsymbol{a}}_i$ stands for the local accelerations, being the second term of the right hand side of equation (2.12). The 3×3 mass matrices $\boldsymbol{m}_i$ contain the body masses m_i on the diagonal. The forces on the right hand side are external forces and reaction forces. In the same way as for translatory motions the angular momentum equations are set up with the mass moment of inertia of each body $\boldsymbol{I}_i$ as follows

$$\boldsymbol{I}_i \cdot \boldsymbol{J}_{Ri} \cdot \ddot{\boldsymbol{q}} + \dot{\boldsymbol{J}}_{Ri} \cdot \dot{\boldsymbol{q}} + \tilde{\boldsymbol{\omega}}_i \cdot \boldsymbol{I}_i \cdot \boldsymbol{\omega}_i = \boldsymbol{l}_i^e + \boldsymbol{l}_i^r. \tag{2.23}$$

Skew-symmetric Matrix $\tilde{\boldsymbol{\omega}}_i$ is assembled from the angular velocity vectors $\boldsymbol{\omega_i}$ with the relationship

$$\tilde{\boldsymbol{\omega}}_i = \begin{bmatrix} 0 & -\omega_1 & \omega_2 \\ \omega_3 & 0 & -\omega_1 \\ -\omega_2 & \omega_1 & 0 \end{bmatrix}. \tag{2.24}$$

It is worth mentioning that all equations have been derived so far for a system without local or time-dependent velocities as they do not appear in the floating wind turbine model. The term $(\dot{\boldsymbol{J}}_{Ri} \cdot \dot{\boldsymbol{q}})$ of equation (2.23) is also called the local angular acceleration $\overline{\boldsymbol{\alpha}}$. In order to obtain a definite description of the mechanical

system, (2.22) and (2.23) are put together according to [11] as

$$\begin{bmatrix} \boldsymbol{m}_i \cdot \boldsymbol{J}_i \\ \vdots \\ \boldsymbol{I}_i \cdot \boldsymbol{J}_{Ri} \\ \vdots \end{bmatrix} \cdot \ddot{\boldsymbol{q}} + \begin{bmatrix} \boldsymbol{m}_i \overline{\boldsymbol{a}}_i \\ \vdots \\ \boldsymbol{I}_i \cdot \overline{\boldsymbol{\alpha}}_i + \tilde{\boldsymbol{\omega}}_i \cdot \boldsymbol{I}_i \cdot \boldsymbol{\omega}_i \\ \vdots \end{bmatrix} = \begin{bmatrix} \boldsymbol{f}_i \\ \vdots \\ \boldsymbol{l}_i \\ \vdots \end{bmatrix} + \overline{\overline{\boldsymbol{Q}}} \cdot \boldsymbol{g} \tag{2.25}$$

with $3p$ scalar equations for momentum and $3p$ scalar equations for the angular momentum. In short formulation remains

$$\overline{\overline{\boldsymbol{M}}}(\boldsymbol{q}) \cdot \overline{\overline{\boldsymbol{J}}}(\boldsymbol{q}) \cdot \ddot{\boldsymbol{q}}(t) + \overline{\boldsymbol{q}}^{\boldsymbol{c}}(\boldsymbol{q}, \dot{\boldsymbol{q}}, t) = \overline{\boldsymbol{q}}^{e}(\boldsymbol{q}, \dot{\boldsymbol{q}}, t) + \overline{\overline{\boldsymbol{Q}}} \cdot \boldsymbol{g}. \tag{2.26}$$

Vector $\overline{\boldsymbol{q}}^{e}$ contains all applied forces acting on the system, while vector $\overline{\boldsymbol{q}}^{c}$ contains the Coriolis-, centrifugal and gyroscopic forces. Whereas Coriolis forces are negligible for the FOWT, gyroscopic forces appear when the rotor having a high angular momentum is rotated about an axis which is not the shaft axis. Consequently, plant oscillations about the y-axis can yield oscillating angular momentums about the z-axis. The term $\overline{\overline{\boldsymbol{Q}}} \cdot \boldsymbol{g}$ representing the vector of reaction forces will not influence system dynamics since these forces are always pointing into a constrained direction. Thus, they are eliminated by multiplying equation (2.26) by $\overline{\overline{\boldsymbol{J}}}^{T}$ from the left according to the Lagrangian principle. $\overline{\overline{\boldsymbol{J}}}$ is the global $2 \cdot 3p \times f$ Jacobi-matrix that consists of the p local $3 \times f$ matrices $\boldsymbol{J}_{Ti}$ and $\boldsymbol{J}_{Ri}$. The result is the f-dimensional description of

$$\boldsymbol{M}(\boldsymbol{q}) \cdot \ddot{\boldsymbol{q}} + \boldsymbol{k}(\boldsymbol{q}, \dot{\boldsymbol{q}}) = \boldsymbol{p}(\boldsymbol{q}, \dot{\boldsymbol{q}}) \tag{2.27}$$

representing the set of equations of motion.

In order to conveniently integrate the gained set of equations it is transformed into state-space by solving for the first derivative of the vector of states

$$\dot{\boldsymbol{x}} = \frac{\partial \boldsymbol{x}}{\partial t} = \begin{bmatrix} \dot{\boldsymbol{q}} \\ \ddot{\boldsymbol{q}} \end{bmatrix} = \begin{bmatrix} \dot{\boldsymbol{q}} \\ \boldsymbol{M}^{-1}(\boldsymbol{p} - \boldsymbol{k}) \end{bmatrix}. \tag{2.28}$$

The $2f$ state vector $\boldsymbol{x}$ includes degrees of freedom and their derivatives $\boldsymbol{q}$, $\dot{\boldsymbol{q}}$. With equation (2.28) the multibody system of the FOWT is given. The next section will deal with the mooring system that keeps the plant in a stationary position. The related forces are externally acting on the MBS in the same way as forces from wind and waves. As they are not a disturbance, however, they are described within this chapter of structural dynamics.

2.2 Mooring line model

The floating spar-buoy is anchored over three slack catenary mooring lines which keep the plant in its rough position. Whereas the lines have the purpose of stabilization for other systems the main element to ensure stability with the spar-buoy is the low center of mass far below the sea water level and the center of buoyancy (COB). The three lines are attached at the fairleads which have a distance of approximately 5 m to the center line of the cylinder. The fairleads lie above the center of mass of the buoy but below the COB. With the horizontal and vertical motion of the platform various static and dynamic effects arise. The static displacement of the platform from the anchor determines static horizontal and vertical forces on the fairleads. These depend highly on the anchor position relative to the platform. Hydrodynamic damping, vortex-induced vibration and vibration of water masses adjacent to the lines are dynamic effects to be mentioned. According to [12] these effects are negligible even for the level of detail of the reference model FAST. The remaining equation is the quasi-static equation for a slack line

$$\frac{d^2y}{dx^2} = \frac{\omega}{H_F} \tag{2.29}$$

relating the line trajectory to the horizontal line force H_F and the line weight per unit length ω. The nonlinear system of equations as analytic solution to (2.29) for a line with zero slope at one end and a part accounting for seabed friction relating horizontal and vertical displacement with horizontal and vertical forces remains according to [12] as

$$\begin{aligned} x_F(H_F, V_F) = L - \frac{V_F}{\omega} \ln \left[\frac{H_F}{V_F} + \sqrt{1 + \left(\frac{V_F}{H_F} \right)^2} \right] + \frac{H_F L}{EA} + \\ \frac{C_B \omega}{2EA} \left[- \left(L - \frac{V_F}{\omega} \right)^2 + \left(L - \frac{V_F}{\omega} - \frac{H_F}{C_B \omega} \right) \max \left(L - \frac{V_F}{\omega} - \frac{H_F}{C_B \omega}, 0 \right) \right] \end{aligned} \tag{2.30}$$

and

$$z_F(H_F, V_F) = \frac{H_F}{\omega} \left[\sqrt{1 + \left(\frac{V_F}{H_F} \right)^2} - 1 \right] + \frac{V_F^2}{2EA\omega}. \tag{2.31}$$

The last part of equation (2.30) returns zero when the anchor tension is greater than zero. When no portion of the line rests on the seabed the equation takes

the form

$$x_F(H_F, V_F) = \frac{H_F}{\omega} \ln \left[\frac{V_F}{H_F} + \sqrt{1 + \left(\frac{V_F}{H_F} \right)^2} \right] - \frac{H_F}{\omega} \ln \left[\frac{V_F - \omega L}{H_F} + \sqrt{1 + \left(\frac{V_F - \omega L}{H_F} \right)^2} \right] + \frac{H_F L}{EA} \quad (2.32)$$

and

$$z_F(H_F, V_F) = \frac{H_F}{\omega} \left[\sqrt{1 + \left(\frac{V_F}{H_F} \right)^2} - \sqrt{1 + \left(\frac{V_F - \omega L}{H_F} \right)^2} \right] + \frac{1}{EA} \left(V_F L - \frac{\omega L^2}{2} \right). \quad (2.33)$$

In the reference model FAST both sets of transcendental equations are solved numerically applying a Newton-Raphson iteration with analytically determined starting points. For the reduced model the same equations are solved offline within Matlab in a pre-processing step.

2.2.1 Implementation in reduced model

The reduced model offers several options for calculation procedures of the line forces. The implicit set of equations for the mooring lines are solved offline for horizontal displacements $x_0 = -35 \ldots 35\,\mathrm{m}$ and vertical displacements $z_0 = -15 \ldots 15\,\mathrm{m}$ of the fairleads relative to the anchor. All mooring system parameters are taken from [2] with the extensional stiffness EA set to zero as is the default setting in the reference model. The resulting forces at the fairleads end of the lines are stored in data tables. Both, horizontal and vertical forces over the displacements are illustrated in figure 2.4. These forces can now be interpolated linearly during a simulation or approximated with linear functions or polynomials. Considering the steady states of the platform which is displaced horizontally by about 15 m for rated wind speeds an approximation can yield significant deviations, see the results in chapter 6.

Now that the magnitudes of the line forces according to the fairleads displacement are calculated the fairleads kinematics have to be found. This means that first the displacement of the anchor coordinate system of each line has to be computed giving the projected horizontal line length as well as the vertical elevation. Overall line forces on the platform also depend on the direction of the lines relative to

the fairleads coordinate system. Thus, the orientation of each anchor coordinate system relative to the fairleads coordinate system has to be calculated. A sketch of the mooring system kinematics is given in figure 2.5. With the projected unstretched line length in the initial undisplaced platform position $L_{unstretched,x}$ the angles β_i, $i = 1 \ldots 3$ are calculated

$$L_{0,cos} = L_{unstretched,x} \cos(60°) \qquad L_{0,sin} = L_{unstretched,x} \sin(60°) \tag{2.34}$$

$$\beta_1 = \arctan\left(\frac{frlds_2}{L_{unstretched,x} + frlds_1}\right) \tag{2.35}$$

$$\beta_2 = \frac{\pi}{2} + \arctan\left(\frac{L_{0,cos} - frlds_1}{L_{0,sin} + frlds_2}\right) \tag{2.36}$$

$$\beta_3 = \pi + \arctan\left(\frac{L_{0,sin} - frlds_2}{L_{0,cos} - frlds_1}\right) \tag{2.37}$$

representing the angle of attack of the horizontal line forces on the fairleads. Consequently, the resulting forces on the platform are given by

$$F_{Lines,x} = -\left[\cos(\beta_1)H_F(1) + \cos(\beta_2)H_F(2) + \cos(\beta_3)H_F(3)\right] \tag{2.38}$$

$$F_{Lines,y} = -[H_F(1)\sin(\beta_1) + \sin(\beta_2)H_F(2) + \sin(\beta_3)H_F(3)] \tag{2.39}$$

$$F_{Lines,z} = -[V_F(1) + V_F(2) + V_F(3)]. \tag{2.40}$$

These forces combine the contributions from line $i = 1 \ldots 3$ and are applied at the origin of the fairleads coordinate system which lies on the platform center line. This modeling is not going perfectly along with the practical realization of the mooring system with the Hywind prototype. As indicated

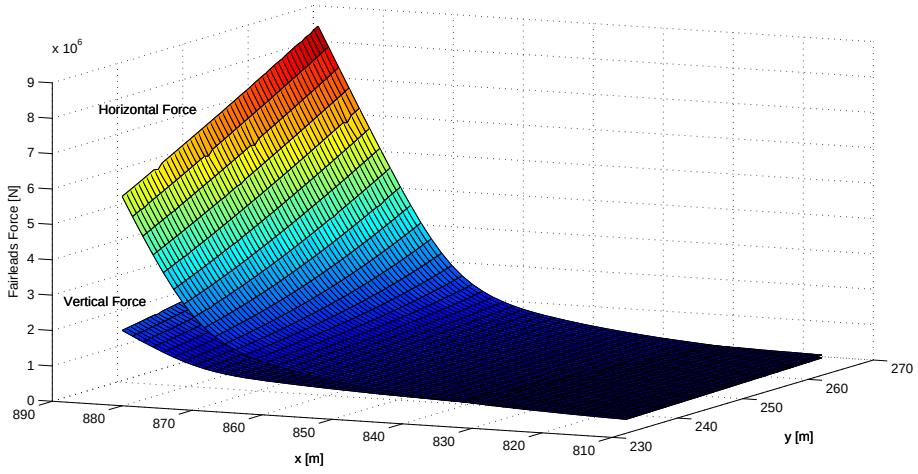

Figure 2.4: Quasi-static mooring model: Horizontal and vertical fairleads forces.

in figure 2.5 the fairleads are attached to the platform at a radius r_{frlds} so that this radius will represent a lever arm to the force and an additional torque $M_{F,y}$ about the fairleads origin arises. Simulations have shown, however, that these torques are small for average platform pitch angles and can be neglected in the following. When applying these external forces on the multibody system equations the resulting torque $\boldsymbol{T}_{Lines}$ about the platform center of mass has to be considered. It is calculated according to equation (2.18) with the position vector of the *frlds*-coordinate system in *ptfm*-coordinates $\boldsymbol{r}_{frlds}^{ptfm}$.

In the next chapter hydrostatic and hydrodynamic forces on the platform are described as well as linear wave theory.

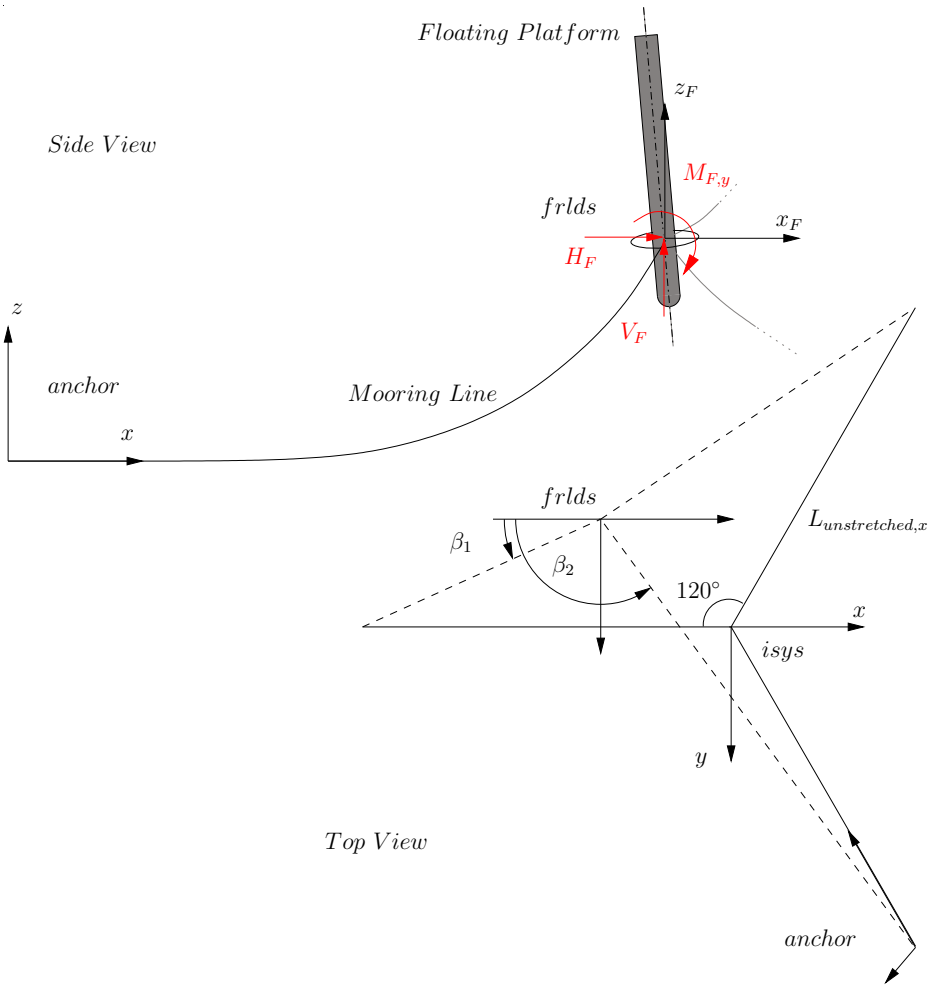

Figure 2.5: Mooring line kinematics.

Chapter 3

Hydrodynamic Model

This chapter describes all forces on the floating spar-buoy that arise from hydrostatics, hydrodynamics and wave loads. Commonly hydrodynamic forces on floating structures are calculated by dividing the problem into three independent parts. The hydrostatic displacement-dependent forces first and subsequently two wave-related problems. One of them is the radiation problem that addresses structure-generated radiating waves and secondly the diffraction problem that assumes a stationary structure that is approached by water waves so that they are diffracted when passing the body. According to [12] the reference model calculates the wave loads as

$$\boldsymbol{F}_{hydro} = \boldsymbol{F}_{hydrostatic} + \boldsymbol{F}_{waves} - \int_0^t \boldsymbol{K}(t-\tau)\dot{\boldsymbol{q}}_{ptfm,swl}(\tau)d\tau. \tag{3.1}$$

The wave force $\boldsymbol{F}_{waves}$ results from the diffraction problem and includes the frequency-dependent wave-excitation vector. The last part is the convolution-integral of the radiation problem with the radiation-impulse-response function $\boldsymbol{K}$. It describes the so-called memory effect that radiating waves have on the platform. The problems are mostly solved in frequency domain in marine engineering so that a commonly computed parameter is the response amplitude operator (RAO) that relates structure amplitudes to a given wave frequency. A drawback of this method is that transient behaviour cannot be considered. Out of this reason the reference model FAST transforms the frequency-domain wave properties into time-domain through an Inverse Fast Fourier Transform (IFFT) so that a time-domain simulation of the comprehensive model can be performed.

The approach for the reduced model calculates hydrostatic forces in the same way as the reference model which is described in the next section. For hydrodynamic forces it uses Morison's equation that has been repeatedly applied for the calculation of marine architecture, see [2]. It is completely written in time-domain and

takes nonlinear damping and added-mass effects into account. All hydromechanic forces on the submerged geometry which are going into the external force vector of Equaton (2.17) are represented by

$$\boldsymbol{F}_{hydro} = \boldsymbol{F}_{hydrostatic} + \boldsymbol{F}_{mor}. \tag{3.2}$$

In order to set up all equations for this simplified estimate of hydrodynamic loads wave kinematics over depth for given wave scenarios have to be calculated. Thus, linear wave theory will be introduced later in this chapter in section 3.2 and the structure loads according to Morison are eventually described in 3.3. Finally, a simplified approach to estimate wave kinematics and the resulting structure loads in time domain is proposed in section 3.4.1.

3.1 Hydrostatics

Static forces fully describe the hydro-structural interface if the water around the platform is still and the platform is in a steady state. The only force that appears in that case is the buoyancy force from Archimedes' principle that exerts on the center of buoyancy of the submerged geometry which coincides with the center of submerged volume. Hydrostatic forces as well as wave-induced forces can be calculated based on geometry-dependent parameters. A software tool to calculate these characteristics is WAMIT (Wave Analysis at MIT, see [14]) which has also been used to calculate input parameters going into FAST. For the calculation of the resulting hydrostatic force

$$\boldsymbol{F}_{hydrostatic} = \boldsymbol{F}_{buoy} - \boldsymbol{C}_{hydrostatic} \cdot \boldsymbol{q}_{ptfm,swl} \tag{3.3}$$

the 6×6 geometry-dependent matrix $\boldsymbol{C}_{hydrostatic}$ is used. It relates the platform degrees of freedom defined at sea water level $\boldsymbol{q}_{ptfm,swl}$ with the resulting hydrodynamic forces and torques about the platform center line at mean sea-level. Made simplifications are the linearization and the assumption that the location of the COB in *ptfm*-coordinates remains constant. According to [12] remains

$$\boldsymbol{C}_{hydrostatic} =$$

$$\begin{bmatrix} 0 & 0 & 0 & 0 & 0 & 0 \\ 0 & 0 & 0 & 0 & 0 & 0 \\ 0 & 0 & \rho g A_0 & 0 & 0 & 0 \\ 0 & 0 & 0 & \rho g \int_{A_0} \zeta^2 dA + \rho g V_0 z_{COB} & 0 & 0 \\ 0 & 0 & 0 & 0 & \rho g \int_{A_0} \xi^2 dA + \rho g V_0 z_{COB} & 0 \\ 0 & 0 & 0 & 0 & 0 & 0 \end{bmatrix} \tag{3.4}$$

with the cross-sectional area of the buoy A_0 and the vertical distance from mean sea-level to the center of buoyancy z_{cob} (< 0) as illustrated in figure 3.1. The diagonal elements of $C_{hydrostatic}$ stand for spring elements in the according direction whereas the off-diagonal elements imply that a displacement of the buoy in a certain direction may yield a displacement or rotation of the platform in another direction. This is not the case here since the platform is axially symmetric. The $(3,3)$-entry is the vertical stiffness that arises from the integration of fluid pressure over the submerged length and gives with the initially submerged volume V_0

$$\boldsymbol{F}_{buoy} = \begin{bmatrix} 0 \\ 0 \\ \rho g V_0 \end{bmatrix}. \tag{3.5}$$

This is the total buoyancy force of the vertically displaced buoy. The $(4,4)$ and $(5,5)$-entries consist of two parts. The first is related to the torque about the platform centerline through waterplane area as indicated by the greyed volume in figure 3.1. The second part has its origin in the buoyancy force that contributes to a moment about the platform centerline once the platform looses its upright position with an angular displacement ψ that denotes here a fictitious angle being any of the three spatial rotational directions. It is worth mentioning that the part coming from waterplane area is far smaller than the other. When taking the mid-point of the platform at SWL as a reference as is done in WAMIT the waterplane area contribution is stabilizing, whereas the moment from buoyancy is destabilizing. This is why $\boldsymbol{C}_{hydrostatic}(4,4)$ and $\boldsymbol{C}_{hydrostatic}(5,5)$ are smaller than zero and therewith destabilizing as a whole. The main restoring moment on the buoy is consequently coming from the low center of mass of the platform which is a main characterizing feature of the spar-buoy floating platform concept.

As mentioned previously in section 2.1.2 the Newton-Euler formalism requires all forces and torques being formulated with the center of mass of each body as reference. The WAMIT convention contradicts this methodology so that a most consistent way to combine the two approaches has to be found. In order to use the original WAMIT parameters published for the OC3-Hywind spar-buoy in [2] all hydrostatic and hydrodynamic torques are written with the SWL as reference. This implies that the initial buoyancy force is input into the multibody system at the SWL. All hydrostatic and hydrodynamic forces, however, yield a moment about the platform center of mass as discussed previously and formulated in equation (2.18) with the lever arm $\boldsymbol{r}_{CM}^{ptfm}$.

Hydrodynamic impacts on the platform are highly influenced by waves so that Airy Wave Theory which is implemented in this code is introduced in the next section.

3.2 Linear wave theory

Ocean waves can have various origins ranging from moving submerged structures that radiate water waves to planetary gravity that results in tidal alternations of the sea level. Most common are, however, waves that result from winds on the water surface. Linear waves with a sinusoidal profile so that mean sea-level (MSL) and still water-level (SWL) coincide are the simplest to being modelled mathematically whereas steeper and braking waves with a higher wave height H to wavelength λ ratio $\frac{H}{\lambda}$ propose significant challenges. Linear waves can be easily described starting from potential flow theory with zero vorticity. According to [2] this model realistically represents waves with negligible effects from flow separation and diffraction. Expressed in non-dimensional numbers this means that the Keulegan-Carpenter number K and the structure-dependent diameter-to-wavelength ratio keep the limits

$$K = \frac{\hat{v}T_p}{D} \leq 2 \qquad \frac{D}{\lambda} \leq 0.2. \tag{3.6}$$

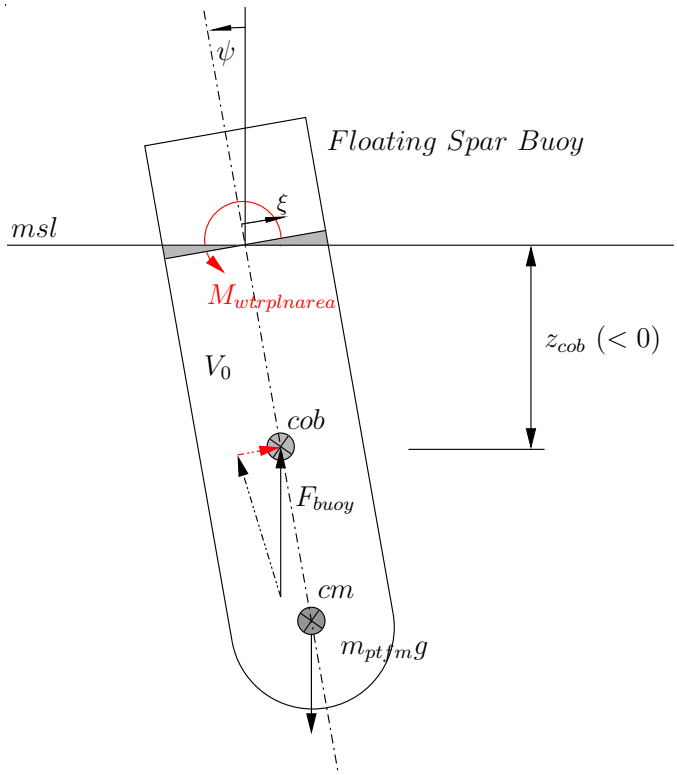

Figure 3.1: Hydrostatic forces and moments on submerged structure.

Whereas K increases for more severe sea conditions the ratio $\frac{D}{\lambda}$ decreases with the severity of the sea according to [2]. For the considered sea states in the latter source up to a significant wave height $H \approx 15\,\mathrm{m}$ with a coupled peak spectral period of $T_p \approx 17\,\mathrm{s}$ this is true and the K-condition from equation (3.6) holds for all but the most severe sea states. The $\frac{D}{\lambda}$-condition, however, is violated for sea states with a short period T_p which is correlated with a small wavelength, see (3.13). The hydrodynamic loads coming from this class of waves is nevertheless negligible because of their small magnitude so that the validity of the linear wave theory can be reduced to the limits of the Keulegan-Carpenter number K.
Potential flow theory is based on the assumption that the water particle velocity

$$\boldsymbol{v} = \nabla\phi \tag{3.7}$$

depends directly on the gradient of the velocity potential ϕ. It is here written in *wave*-coordinates, which coincide with *isys*-coordinates except that the first axis is pointing to the wave propagation direction. The boundary-value problem is solved according to [15] giving a kinematic boundary condition at the free surface and at the sea floor. The dynamic free surface condition results from the nonlinear Bernoulli-equation

$$\left\{ \frac{\partial\phi}{\partial t} + g\eta + \frac{1}{2}V^2 \right\} \Bigg|_{z=\eta} = 0 \tag{3.8}$$

which is linearized by truncating the dynamic pressure term yielding the free surface elevation

$$\eta = -\frac{1}{g}\frac{\partial\phi}{\partial t}\Bigg|_{z=\eta}. \tag{3.9}$$

The linearization of this boundary condition is justified by the observation that the water particle velocity itself is small which leads to a quadratically small value that is negligible compared to the terms of specific gravitational energy and static pressure.
A travelling or progressive wave with a sinusoidal free surface elevation is described by

$$\eta = \frac{H}{2}\cos(k(x - ct)) \tag{3.10}$$

with the celerity or wave propagation velocity c and the wavenumber

$$k = \frac{2\pi}{\lambda} = \frac{2\pi}{cT}. \tag{3.11}$$

With the continuity condition equation (3.7) is solved applying a product solution according to [15] giving

$$\phi = \frac{H}{2}\frac{g}{\omega}\frac{\cosh[k(z+h)]}{\cosh(kh)}\sin(kx - \omega t). \tag{3.12}$$

Now, the water particle velocities over depth for a given significant wave height H can be calculated by simply integrating equation (3.12) in space. The relationship between the wave frequency ω and the wave length λ can also be found at this point combining (3.11) and (3.12) resulting in the implicit dispersion relationship

$$\omega = \sqrt{gk \tanh(kh)}. \tag{3.13}$$

The second part of equation (3.11) shows that the wave propagation velocity c depends directly on the wavenumber k which on the other hand is not a constant unless waves consist of a single frequency which would then be a so-called regular wave. Since the fluid model used here is irrotational it is also non-diffusive. This is actually unphysical since small eddies would realistically be transformed into heat at some point. Here they are "dispersed" or continuously transported at the according velocity. Looking at the fluid particle velocities and accelerations over water depth it can be seen in figure 3.2 how they decay exponentially over depth. Water particles do not travel with a wave but follow elliptic orbits so that the overall position of fluid particles remains roughly constant as long as no currents exist. In order to account for impacts from fluid above SWL several so-called stretching methods exist. These extend fluid kinematics above the domain of definition of (3.12) for wave heights $\eta > 0$. This can be observed in figure 3.2 on the right. With the herein applied vertical stretching method, the velocities and accelerations at SWL are also assumed to remain constant above SWL.

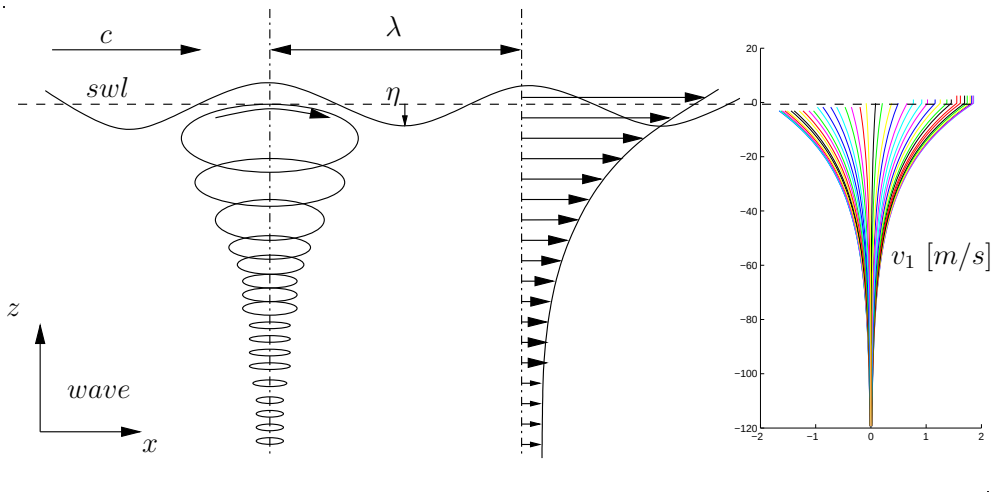

Figure 3.2: Wave kinematics.

At this point we have completed the set of equations to describe wave kinematics over depth for a specific wave frequency. Realistic wave scenarios, however, include waves of various frequencies and wavelengths. Two prevalent wave spectra are the one determined by the Joint North-Sea Wave Project (Jonswap) and

the Pierson-Moskowitz Spectrum which is implemented in this work. Figure 3.3 shows a one-sided wave spectrum with a peak spectral period $T_p = 10\,\mathrm{s}$ and a significant wave height of $H_s = 6\,\mathrm{m}$.

Such a wave is dispersive which means that the celerity varies for each frequency

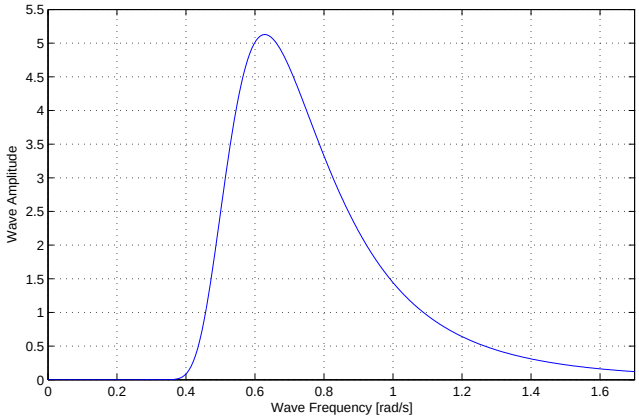

Figure 3.3: Pierson-Moskowitz wave spectrum.

as can be seen in equation (3.11). Out of this reason the wave kinematics cannot be calculated in time-domain according to equation (3.12). The wave heigth H with its associated sinusoidal time-domain variation is rather replaced by the introduced spectrum so that equation (3.12) is written in frequency domain and integrated in space to obtain the horizontal fluid particle velocity

$$v_{f,1}(t,x,y,z) = \frac{\cos(\beta)}{2\pi}\int_{-\infty}^{\infty} W(\omega)\sqrt{2\pi S_\eta^{2sdd}(\omega)}e^{-ik(\omega)[x\cos(\beta)+y\sin(\beta)]}\omega \frac{\cosh[k(\omega)(z+h)]}{\sinh[k(\omega)h]}e^{i\omega t}d\omega. \quad (3.14)$$

The horizontal velocity, v_2, perpendicular to v_1 is calculated accordingly with the angle β towards the positive x-axis in *wave*-coordinates. It indicates the wave propagation direction. The vertical fluid velocity is not influenced by β and shows only a difference to (3.14) in the hyperbolic fraction since (3.12) has to be integrated in z-direction instead of x-direction

$$v_{f,3}(t,x,y,z) = \frac{i}{2\pi}\int_{-\infty}^{\infty} W(\omega)\sqrt{2\pi S_\eta^{2sdd}(\omega)}e^{-ik(\omega)[x\cos(\beta)+y\sin(\beta)]}\omega \frac{\sinh[k(\omega)(z+h)]}{\sinh[k(\omega)h]}e^{i\omega t}d\omega. \quad (3.15)$$

Vector $W(\omega)$ stands for the Fourier Transform of white gaussian noise with unit variance which is needed for the inverse Fourier Transform. It is calculated applying the Box-Muller Method taken from [1]. The *isys*-coordinates x

and y define the horizontal location of the computed kinematics over depth so that (3.14) and (3.15) eventually serve to compute a three-dimensional vector field of fluid velocities. For the inverse discrete Fourier Transform that is applied on the integrand in equations (3.14) the two-sided amplitude spectrum S_η^{2sdd} is needed. The reason for this is that a two-sided spectrum that is conjugate-symmetric results from a FFT on a time signal. Conjugate-symmetric means that e.g. $S(2) = conj(S(n-1))$ is valid with $S \in \mathbb{C}^{n\times 1}$. Now that the target is to obtain a real-valued time signal out of a given spectrum for the free surface elevation the spectrum input into the IFFT needs to be conjugate-symmetric as well. The realization of the IFFT in my Matlab function *MFloater_Airy.m* uses a two-sided spectrum with

$$S_\eta^{2sdd}(\omega) = \begin{cases} \frac{1}{2} S_\eta^{1sdd}(\omega) \text{ for } \omega \geq 0 \\ \frac{1}{2} S_\eta^{1sdd}(\omega) \text{ for } \omega < 0 \end{cases} \tag{3.16}$$

and makes use of the discrete IFFT-algorithm included in Matlab with the option *symmetric*. By doing so only the first half of entries of $S_\eta^{2sdd}(\omega)$ are regarded as relevant entries and the result is a real-valued time signal of the wave height. Figure 3.4 shows a time-series plot of an irregular wave with $Tp = 10\,\text{s}$ and $H = 6\,\text{m}$ on top. The evolution over depth of the horizontal fluid particle velocities for the same wave is depicted in the center. At the bottom of figure 3.4 the free surface elevation signal is transformed back into frequency domain to show that the wave spectrum of the computed time-series turns out as previously defined in figure 3.3.

With the time-domain wave kinematics of linear waves defined it is now possible to estimate the resulting wave loads on the platform.

3.3 Reduced model hydrodynamic loads

Various models exist to calculate dynamic marine fluid-structure interactions. A simplest and for bottom-mounted oil and gas constructions highly validated model in time-domain is Morison's equation. The equation in its relative formulation uses semi-empirical parameters to relate water kinematics over depth as well as structure kinematics with the resulting forces on the submerged body. The model neglects effects from flow-separation and diffraction. The radiation problem includes a damping effect and an added-mass effect which result in phase-lagged reactive forces by water particle motions which are induced by the structure motion itself. This memory-effect is neglected in this formulation. Diffraction appears for severe sea-states with a Keulegan-Carpenter number $K > 2$, as discussed in section 3.2 and is negligible for the spar-buoy in most relevant sea-states.

For the reduced FOWT model the hydrodynamic inputs are modelled through the relative form of Morison's equation resulting in a force in $k = 1$ and $k = 2$-direction of the *ptfm**-coordinate system that is identical to *ptfm* but has a constant *isys*-orientation. Thus, the force reads,

$$F_{mor,k} = \rho \frac{\pi D_{bT}^2}{4} \int_{z_1}^{z_2} -C_A a_{b,k}(z) + (1 + C_A) a_{f,k}(t, z) dz + \frac{1}{2} C_D \rho D_{bT} \int_{z_1}^{z_2} [v_{f,k}(t, z) - v_{b,k}(z)] |\boldsymbol{v}_f(t, z) - \boldsymbol{v}_b(z)| dz. \quad (3.17)$$

The numerical integration is done in vertical direction with the center of mass of the platform as reference from the bottom end of the platform $z_1 = z_{CM} - z_{buoy}$ up to $z_2 = z_{CM} - q_3$ which is the location of the sea water-level in *ptfm*-coordinates. According to [12] Morison's equation is usually applied only up to SWL so that no stretching method is necessary. However, simulations have shown that the effect of stretching is very low for common sea-states. This form of vertical slicing of a submerged structure is an application of strip-theory that is a common technique in the field of marine engineering. The first part of equation (3.17) is the added-mass term which returns the forces arising through fluid masses oscillating with the platform. The included parameters in that term are taken from the OC3-Hywind reference FOWT [2] with an added-mass coefficient $C_A = 0.969954$ so

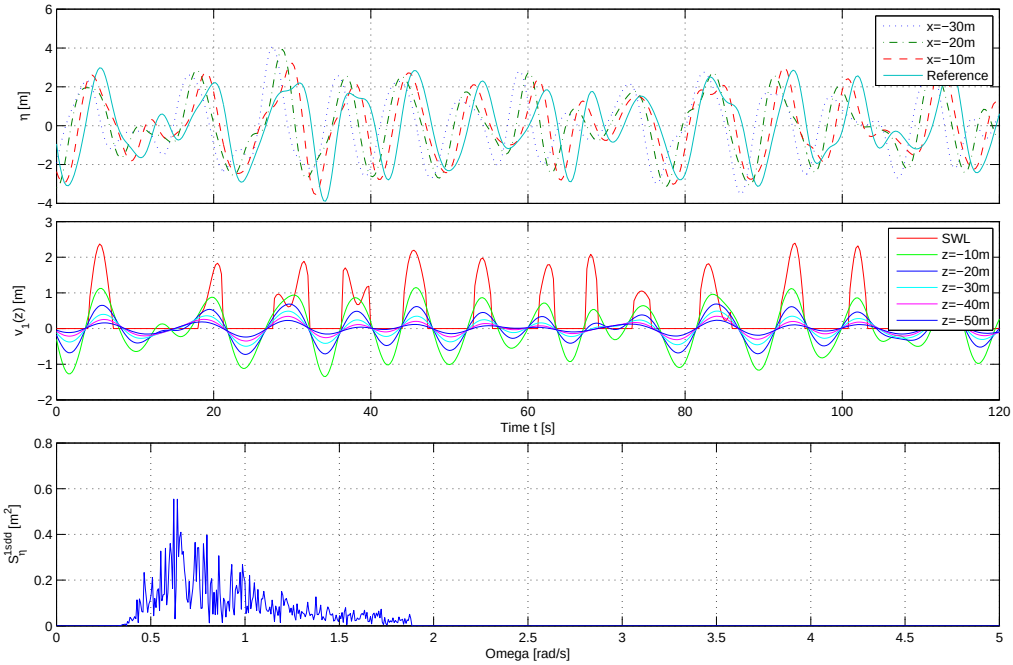

Figure 3.4: Wave elevation at four points on x; Fluid particle velocities in x-direction over depth; Back-transformed wave spectrum $S_\eta^{1sdd}(\omega)$.

that the oscillating fluid mass is assumed to almost equal the one that would fit into the buoy cylinder of diameter D_{bT}, see figure A.1. Therefore the absolute acceleration of the platform body over depth $a_{b,k}(t,z)$ in inertial coordinates is needed. As the acceleration is not a state of the multibody system equations of motion (2.27) the differentiated state vector is only available after having solved the right hand side of (2.28). A solution for this numerical problem is proposed in section 3.3.1. For the second part of equation (3.17) fluid particle accelerations over depth are needed. Therefore the equation for the velocity (3.14) of linear wave theory needs to be differentiated yielding

$$a_{f,1}(t,x,y,z) = \frac{i\cos(\beta)}{2\pi}\int_{-\infty}^{\infty} W(\omega)\sqrt{2\pi S_\eta^{2sdd}(\omega)}e^{-ik(\omega)[x\cos(\beta)+y\sin(\beta)]}\omega^2 \frac{\cosh[k(\omega)(z+h)]}{\sinh[k(\omega)h]}e^{i\omega t}d\omega. \quad (3.18)$$

The last term of equation (3.17) is velocity dependent and represents both, hydrodynamic damping and velocity-dependent wave loads. Consequently, Morison's equation models not only wave loads but also hydrodynamic damping and added-mass forces at still sea. The vectorial platform velocity at each strip at depth z in inertial coordinates is calculated by

$$\boldsymbol{v}_b(z) = \dot{\boldsymbol{r}}_{ptfm} + \boldsymbol{\omega}_{ptfm} \times \left(\boldsymbol{S}_{ptfm} \cdot \boldsymbol{r}_z^{ptfm}\right) \quad (3.19)$$

using kinematic functions of the multibody system equations, see equation (2.3). The small portion of the body strip velocities $\boldsymbol{v}_b(z)$ in z-direction is considered negligible so that equation (3.17) is scalar for the two horizontal directions. The contribution from motions in z-direction by both, structure and fluid particles, is taken into account by the vectorial magnitude of equation (3.17). It is mentioned that the reduced model includes additional damping in surge-, sway- and heave direction in the same way as the reference model FAST. The numerical values for this additional linear damping are given in [2].

3.3.1 Integration into multibody system equations

As stated before it is necessary to describe applied forces on the bodies of the multibody system as forces and torques about the respective center of mass. Thus, the center of the distributed hydrodynamic load needs to be found so that the resulting moment about the platform center of mass can be calculated. The resulting moment remains as follows

$$M_{mor,k} = \int_{z_2}^{z_1} z\, dF_{mor,l} \qquad \text{with} \qquad k,l \in \{1,2\},\ k \neq l. \quad (3.20)$$

Morison's equation is a simple way of estimating hydrodynamic loads on a structure in time-domain. However, there are two drawbacks in a numerical point of view. First, a numerical integration is costly in terms of computational effort. A solution to this is proposed in the next section. Second, the acceleration of the multibody system is needed to calculate the external force. Regarding equation (2.28), the derivative of platform states $\dot{\boldsymbol{q}}$ that includes the second derivative of the degrees of freedom is the variable being solved for which goes into the numerical integration algorithm. Consequently, the needed accelerations are only available delayed by one time-step. This lag of dynamic forces can result in numerical instability also because the accelerated fluid mass is even greater than the platform mass itself. Out of this reason the first term of equation (3.17) is already included as part of the multibody system equations (2.27) in the mass matrix

$$\boldsymbol{m}^*_{ptfm} = \begin{bmatrix} m_{ptfm} + m^* & 0 & 0 \\ 0 & m_{ptfm} + m^* & 0 \\ 0 & 0 & m_{ptfm} \end{bmatrix} \tag{3.21}$$

with the added mass

$$m^* = \rho \frac{\pi D_{bT}^2}{4} C_A z_{buoy} \tag{3.22}$$

with the full platform diameter below the taper D_{bT}. By augmenting the inertial mass of the system this way the dynamics in z-direction are not influenced. With equation (3.21) only translatory accelerations at the platform center of mass are taken into account, whereas high translatory accelerations for strips far away from the center of mass can arise through platform rotations. Thus, the mass moment of inertia of the platform is modified in the same way as the inertial mass. It results as

$$\boldsymbol{I}^*_{ptfm} = \int_{-z_{buoy}}^{0} \rho \frac{\pi D_{eff}^2}{4} C_A z^2 dz. \tag{3.23}$$

Here, unlike in equation (3.21) an effective diameter of the buoy, D_{eff} is used that equals the platform diameter above the taper. Simulations with these settings showed better agreement with the reference model FAST in free-decay simulations with an initial *PtfmSurge*-displacement.

3.4 Simplified hydrodynamics

In this section an approach is introduced to simplify the equations for the wave kinematics over depth of linear Airy Wave Theory. The main problem of equation (3.12) coupled with Morison's equation (3.17) for this application is that it requires three-dimensional fluid particle velocities and accelerations over depth and time. This means that the disturbance of the waves cannot be measured in a feasible way, which was one of the targets of this project. Another

issue is that equation (3.17) needs to be integrated over all structure strips or sea depth, respectively. During an analysis of computational time of the reduced model code it turned out that the numerical integration consumes more than half of the simulation time. Out of this reason a simplified estimation of the fluid particle kinematics of equation (3.14), (3.15) and (3.18) is sought. Thus, the evolution of wave kinematics over depth can be estimated based on the free surface elevation η, only. With this estimation it is finally possible to reduce the complexity of the disturbance model and to avoid the numerical integration over depth so that each term of Morison's equation can be integrated analytically as described in section 3.4.2.

3.4.1 Simplification of linear wave model

Equation (3.12) for the velocity potential of a single frequency wave includes the current wave height which can be described as a timeseries for a regular wave as

$$\eta = \frac{H}{2} sin(kx - \omega t). \tag{3.24}$$

This linear dependency on η is lost when rewriting the formulation for the wave velocities over depth for irregular waves, see equation (3.14). Irregular waves imply that not only one wave frequency is considered but a spectrum over a range of frequencies. In the case of irregular waves the free surface elevation η is part of the integral of the IFFT because the current wave height depends on the wave frequency or the wavelength $\lambda = \frac{2\pi}{k}$ in the same way as the function over depth of the fluid velocities, equation (3.12), does. For a simplified estimation of wave loads with the eventual goal of a real-time application the velocity (and acceleration) distribution of water particles over depth needs to be estimated based on the current wave height, only. Consequently, the question arises how the wave frequency characteristics like λ or k are estimated so that equations (3.24) and (3.14) can be solved. Considering the wave spectrum, like the one in figure 3.3 it is a plausible option to base the estimation on the peak spectral frequency and the according wavelength returned by relationship (3.13). Another conceivable procedure is to estimate current wave properties through a real-time FFT of sequentially recorded timeseries. Apart from estimations aiming at real-time measurements there is to mention the possibility of regarding the eigenfrequency of the platform of about $f_{eig,ptfm} \approx 0.05\,\mathrm{Hz}$, see [16] in order to focus on excitation frequencies relevant to the specific dynamic platform characteristics. However, the wavelength that is correlated with this eigenfrequency is $\lambda \approx 623\,\mathrm{m}$ which is far longer than the characteristic length of the buoy. Also, the angular frequency $\omega_{eig,ptfm} \approx 0.31\,\mathrm{rad/s}$ does not appear in the Pierson-Moskowitz-Spectrum, figure 3.3, which has been a design criterion

for the spar-buoy concept. These two facts lead to the assumption that it is far more sensible to focus on the peak frequency that actually appears in the spectrum instead of the eigenfrequencies.

In a first approach the velocity distribution over depth as seen in figure 3.2 has been approximated by an exponential function which depends linearly on the wave height instead of the hyperbolic fraction of equation (3.12). The form

$$v_{f,1}(\eta, z) \approx a_{v_1} \eta e^{b_{v_1} z} \tag{3.25}$$

has been used for a numerical optimization to find the unknown coefficients a_{v_1} and b_{v_1} for the case of horizontal velocities in x-direction. Therefore Airy's function for $v_{f,1}$ for various wave heights η is taken as target and an exponential function with a_{v_1} as one and b_{v_1} as the other optimization variable fitted to it. The two-step optimization has been performed for all wave heights within a period of a regular wave with $H = 6\,\mathrm{m}$. The analysis has only been done for a wave period of $T_p = 10\,\mathrm{s}$ which is assumed to be the peak spectral period of the spectrum. Fluid particle velocities in vertical direction as well as accelerations in x-direction do not have an explicit dependency on the wave height as can be seen in figure 3.2. Since both are phase-lagged by 90° to the free surface elevation it is possible to use the time-derivative of the free surface elevation as coefficient so that results

$$v_{f,3}(\eta, z) \approx a_{v_3} \frac{d\eta}{dt} e^{b_{v_3} z} \qquad \text{and} \qquad a_{f,1}(\eta, z) \approx a_{a_1} \frac{d\eta}{dt} e^{b_{a_1} z}. \tag{3.26}$$

A similar simplification of the original formulation of Airy Wave Theory is given in literature for shallow and deep water. This simplification also results in an exponential function that replaces the hyperbolic fraction of equation (3.12). The approximation for deep water is valid for $2h > \lambda$. The water depth assumed for this study is $h = 320\,\mathrm{m}$ and the peak wavelength of the Pierson-Moskowitz Spectrum is $\lambda \approx 156\,\mathrm{m}$ so that the approximation is valid here. It is valid up to a wave period of $T^{deepw,max} = 20.4\,\mathrm{s}$ for the given ocean depth. Finally, deepwater approximation assumes that the following relationship holds

$$\sinh(kh) \approx \cosh(kh) \approx \frac{1}{2} e^{kh} \tag{3.27}$$

for deep water conditions. Thus, the integral of equation (3.12) with respect to the indicated directions with a subsequent replacement of the hyperbolic functions

using equation (3.27) yields

$$v_{f,1}(H,\omega,z,t) = \frac{H}{2}\omega e^{kz}\cos(kx-\omega t) \tag{3.28}$$

$$v_{f,3}(H,\omega,z,t) = \frac{H}{2}\omega e^{kz}\sin(kx-\omega t) \tag{3.29}$$

$$a_{f,1}(H,\omega,z,t) = \frac{H}{2}\omega^2 e^{kz}\sin(kx-\omega t). \tag{3.30}$$

This description is formulated as in common literature for a given sinusoidal profile for η and not with respect to the current wave height and its derivative as in the first approach, equations (3.25) and (3.26). Such a description is, however, necessary for the real-time application with measurable inputs.

The functions for the simplified wave kinematics as introduced in the first place, see equation (3.26), depend on the parameters a_{v_i}, a_{a_1}, b_{v_i} and b_{a_1} and the actual free surface elevation η and its derivative. Equations (3.28) to (3.30) on the other hand contain the wave angular frequency ω as well. Out of this reason, deepwater approximation needs to be reformulated accordingly. Eventually, the wave kinematics functions according to linear wave theory with deepwater approximation are written as in equations (3.25) and (3.26), dependent on the free surface elevation η and its derivative $\frac{d\eta}{dt}$. The according coefficients are collected in table 3.1.

Table 3.1: Parameters of simplified functions for wave kinematics, equation (3.25) and (3.26) for $T_p = 10\,\mathrm{s}$

Horizontal velocity	a_{v_1}	$= \omega_p$	≈ 0.6283
	b_{v_1}	$= k_p$	≈ 0.0403
Vertical velocity	a_{v_3}	$= \frac{\omega_p}{\omega_p}$	$= 1.0$
	b_{v_3}	$= k_p$	≈ 0.0403
Horizontal acceleration	a_{a_1}	$= \omega_p$	≈ 0.6283
	b_{a_1}	$= k_p$	≈ 0.0403

All coefficients of table 3.1 are calculated for the specific peak spectral period $T_p = 10\,\mathrm{s}$. It is shown, however, that all coefficients depend on ω_p and k. Therefore, deepwater approximation has been implemented in the reduced model code as a function of a considered wave angular frequency ω_p.

The performance of this approximation is analyzed in section 3.5, where also a prediction of wave loads based on buoy-wave height measurements is evaluated. In the following an analytical form of Morison's equation is described.

3.4.2 Analytical calculation of hydrodynamic loads

With the approximated exponential functions for fluid particle motion over depth found in the previous section it is possible to avoid the numerical integration of Morison Equation (3.17). In the following the process to calculate wave loads directly based on simplified linear wave theory is shown. Morison's equation remains with the simplified fluid velocities and accelerations as

$$F^*_{mor,k} = \rho\frac{\pi D^2_{bT}}{4}\int_{z_1}^{z_2} -C_A a_{b,k}(z) + (1+C_A)a^*_{f,k}(\eta,z)dz + \frac{1}{2}C_D\rho D_{bT}\int_{z_1}^{z_2}[v^*_{f,k}(\eta,z) + v_{b,k}(z)]dz. \quad (3.31)$$

Besides the replacement of the original fluid kinematics functions with the *-denoted exponentials the contribution from vertical fluid and structure motion, $|\boldsymbol{v}_f(t,z) - \boldsymbol{v}_b(z)|$, has also been neglected. It is mentioned that this is also the case in the original publication by J.R. Morison, see [17]. With the splitting of the integral and the now possible analytical integration of fluid kinematics functions the platform kinematics can also be integrated analytically. Therefore body velocity and acceleration over the buoy length is divided into a translational term that is constant for all strips and a linear part from rotational motion. For the velocity results

$$\int_{z_1}^{z_2} v_{b,1}(z)dz = \boldsymbol{q}_1(z_2 - z_1) + \frac{1}{2}\dot{\boldsymbol{q}}_5(z_2^2 - z_1^2) \quad (3.32)$$

with the derivative of the platform-surge degree of freedom $\boldsymbol{q}_1$ and the derivative of the platform pitch degree of freedom $\dot{\boldsymbol{q}}_5$. In order to calculate the moment about the platform center of mass resulting from the Morison-force the different area load terms related to platform and wave velocity as well as platform and wave acceleration are integrated separately. For the moment resulting from the platform velocity term of equation (3.31) remains

$$M^*_{mor,b1} = C_A l_{buoy}\rho\frac{\pi D^2}{4}\int_{z1}^{z_2} v_{b,1} z dz. \quad (3.33)$$

With this procedure a method is given to calculate the overall loads on the floating structure which saves a large quantity of computational time.

3.5 Prediction of wave loads

The eventual goal of this project is to optimize controller activity based on disturbance information for a time frame in the future as well as the equations

of motion of the plant itself. Whereas wind information is available from LIDAR measurements, see chapter 4, wave loads have to be measured by any kind of device observing the wave height on a spot, a line or over an area. Direct measurements of wave kinematics seem difficult due to high turbulence and the elliptic trajectory of fluid particles. Measuring the free surface elevation on a line ahead of the plant in negative wave propagation direction will return an integral wavelength information instantly. Through the dispersion relationship (3.13) wavelength information might be alternatively found through an FFT of the wave height on a spot within a time window which is, however, not instantly available. These kinds of estimates will eventually be needed for the calculation of wave kinematics when one does not rely on previously measured peak spectral data as has been done for the simplified fluid kinematics functions, see section 3.4.1. Besides the issue of obtaining the latter functions it is also necessary to estimate the wave propagation velocity, see equation (3.11), when the measurement device is located ahead of the platform. In this work wave input is assumed to come from a buoy on a spot in negative wave direction.

Figure 3.5 shows the Morison torque about the platform center of mass, see equation (3.20), for an irregular wave with peak spectral period $T_p = 10\,\mathrm{s}$ and a significant wave height $H_s = 6\,\mathrm{m}$ on the stationary platform. Whereas the black line represents the exact torque calculation according to Morison the blue line is based on the estimation described in the last section with measurements of the wave height at the same platform location. The dotted and dashed lines show the results of the wave kinematics estimate that is now based on buoy measurements ahead of the platform. In this case the wave propagation velocity is estimated using the same wavenumber $k_p = 0.0403$ related to $T_p = 10\,\mathrm{s}$ as before. The second part of figure 3.5 shows a coherence plot between the hydrodynamic platform moment based on the original Morison Equation and the various estimates through buoy input. It can be seen that waves of the main frequency $f_p = 0.1\,\mathrm{Hz}$ give a high agreement of the estimates whereas other frequencies show deviations. The cut-off frequency in the coherence plots is $f_{cut} \approx 0.6\,\mathrm{Hz}$ even without estimation of celerity. It is noticeable that the closer the measurement buoy is to the platform the better is the agreement in the relevant range of frequencies, see figure 3.3.

In summary the previously presented estimates include first an estimation of a prevailing peak frequency for the calculation of wave kinematics, second a simplification of the hyperbolic fraction of e.g. equation (3.14) to a simple exponetial and lastly the estimate of propagation velocity which all depend on the wave frequency. Considering this high level of simplification the presented results are promising since the estimates still coincide roughly with the exact solution even

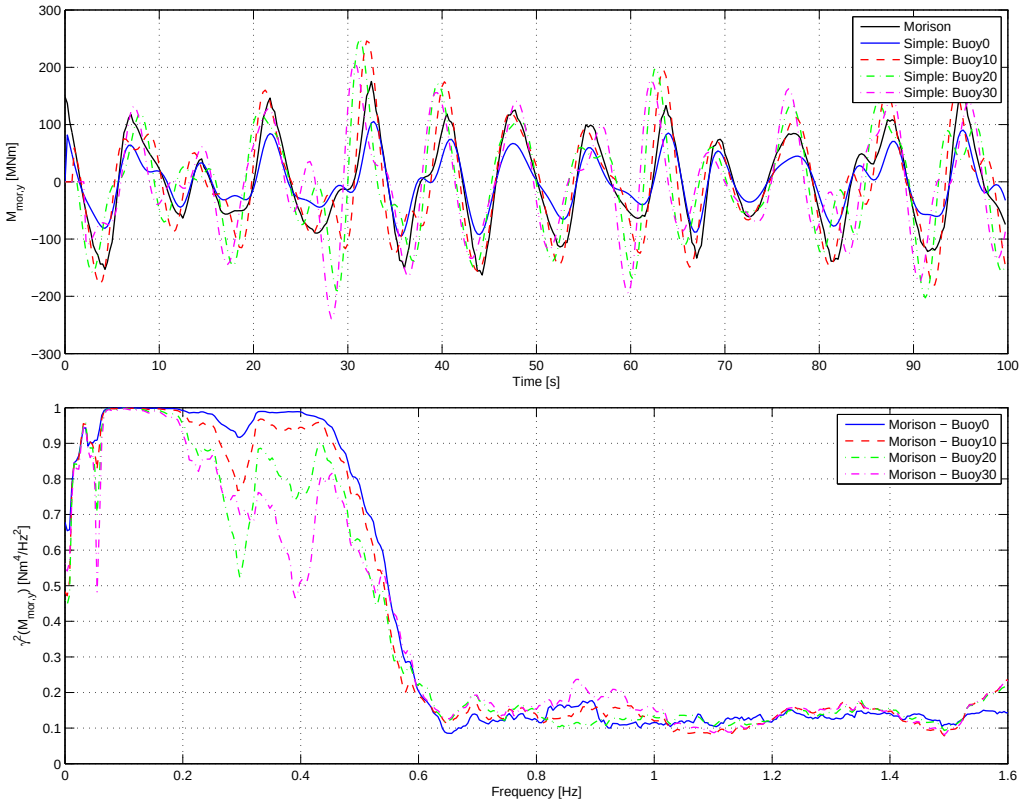

Figure 3.5: Verification of simplified wave kinematics model comparing structure loads.

for distant measurements and improve significantly when getting closer to the platform. This fact is very useful for the application within NMPC.
With this the description of hydrodynamics is completed so that the other disturbance on the FOWT coming from aerodynamics can be addressed in the next section.

Chapter 4

Aerodynamic Model

Various models exist to calculate the aerodynamic forces on a rotor. Most of them have their origin in the field of aerospace engineering and the study of airfoils. With mostly empirically measured coefficients for the lift and drag of a rotor blade it is possible to calculate the forces resulting from a circumventing airflow. Most of these models aim at optimizing the power output of the wind turbine through an optimal shape of the blade or a good or predeterminable performance in a certain range of wind speeds. The reference model FAST applies the Blade Element Momentum Theory (BEM). This is an iterative approach that bases on the conservation of momentum coupled with the mentioned coefficients. The airflow around the blade is calculated with a given three-dimensional vector field of wind speeds ahead of the rotor. Such turbulent wind fields can be simulated by tools like TURBSIM, see [18]. The following section will address the aerodynamic method for airfoil kinetics as used in FAST, shortly.

4.1 Blade Element Momentum Theory

Resulting forces and torques on a rotating wind turbine rotor cannot be calculated in a direct way from rotor and fluid velocity as for closed turbomachinery like classical steam or hydro turbines. The reason for this is that the flow field expands radially when passing the rotor-plane. According to the Froude-Rankine theorem, the axial fluid velocity in the rotor-plane is exactly the average of the wind speeds far ahead and far behind the rotor plane. Therefore, the convention holds in rotor blade theory to use the indices 1, 2 (or none) and 3 for aerodynamic quantities in front of, in and behind the rotor plane. The conservation of momentum in flapwise direction of a flow passing a radial section dr at the angle of attack α of

a blade with depth t takes the form

$$dF_L = 2\pi r \rho dr\, c \sin(\alpha) \tag{4.1}$$

with the absolute velocity in the rotor plane c, see [13]. Now information about the lifting properties c_L of the blades from rotor disk theory

$$dF_L = \frac{\rho}{2} c^2 t\, dr\, c_L(\alpha_A) \tag{4.2}$$

is added where α_A is the relative portion of the angle of attack with respect to the edgewise direction. Subsequently, equation (4.1) and (4.2) are combined which results according to [13] in

$$t c_L \alpha_A - \frac{8\pi r}{z} \sin(\alpha) \tan(\alpha_1 - \alpha) = 0. \tag{4.3}$$

This equation has to be solved numerically in order to find the fluid angle of attack α for each radial section of the blade. More detailed correction models exist in most numerical codes for flow conditions that differ significantly from the design point so that complex phenomena like flow separation occur.

Here, the main focus is to find a simplest and computationally cheapest method to estimate all forces and torques on the wind turbine hub. The method proposed by [9] for NMPC using LIDAR measurements, see [19], on onshore wind turbines is widely adopted for the reduced model. Within this application the wind speed is measured by a laser system on the nacelle via the doppler effect so that a frequency shift occurs that is related to the line-of-sight speed of the reflecting air particles. The wind speeds are measured on circular trajectories in various distances to the rotor plane and subsequently reduced to a scalar wind speed v_0 in shaft direction at hub height. The calculation of the resulting force according to the wind speed and the rotor angular speed as well as blade pitch angles, how it is realized in the reduced model code, is derived in the following.

4.2 Reduced model aerodynamic loads

Main loads on the rotor hub is the aerodynamic torque about the shaft axis and the thrust force from blade drag in shaft direction. These kinetics depend on the relative rotor effective wind speed taking the movement of the rotor coordinate system into account through

$$v_{rel} = -\dot{\boldsymbol{r}}_{rotor}(1) - v_0. \tag{4.4}$$

The rotor-effective wind speed $v_0 > 0$ results from a simplification of the three-dimensional turbulent vector field ahead of the rotor. The method presented

by [9] is a weighted averaging of horizontal wind speed components over the rotor plane. The weighting function takes the varying deceleration of wind speeds at different radii into account. A variable that has significant effects on the forces on the rotor blades is the tip-speed ratio

$$\lambda = \frac{\Omega R}{v_{rel}} \tag{4.5}$$

and the blade pitch angle θ. For the aerodynamic torque results

$$M_{aero} = -\frac{1}{2}\rho\pi R^3 \frac{c_P(\lambda,\theta)}{\lambda} v_{rel}^2 \tag{4.6}$$

with the rotor radius R and the nondimensional torque coefficient c_P. The thrust force depends on the rotor effective wind speed in second order as

$$F_{aero} = -\frac{1}{2}\rho\pi R^2 c_T(\lambda,\theta)\lambda v_{rel}^2 \tag{4.7}$$

with the thrust coefficient c_T that is also nondimensional. Whereas the power coefficient c_P reaches a peak ($c_{p,max} < \frac{16}{27}$) at $\lambda \approx 8$ the thrust coefficient c_T increases steadily in a nonlinear fashion. Drag forces on the blades influencing c_T as well as lift forces on the blades influencing c_P depend highly on the blade pitch angle, especially in the range of angles where stall occurs. For further illustration of these dependencies, see [9]. There are various aerodynamic effects that are neglected with this reduced model. As already mentioned in the previous section flow separation is assumed not to appear which is true for conditions around the operating point. Apart from this, effects of dynamic inflow, see [20], are not considered. As the floating wind turbine has far more rotational degrees of freedom than the onshore wind turbine or the fixed-bottom offshore WT the possibility of oblique inflow is more likely to occur. Out of this reason these effects of a non-alignment of the rotor towards wind speed on the aerodynamic coefficients is further analyzed in the next section.

4.3 Oblique inflow model

As a basis for the assessment of the effects of rotor misalignment the FAST code has been used. A script performing a loop of steady-state simulations has been made in order to calculate the torque and thrust coefficients for various yaw errors. Figure 4.1 shows the dependency of c_P and c_T on the yaw error. Their calculation is based on F_{aero} and M_{aero} with the rotor effective wind speed in horizontal direction v_{rel}. It can be seen that oblique inflow has the biggest impact for high tip-speed ratios in the case of c_T and for maximum values of c_P. In figure 4.2 the coefficients are shown for different yaw errors but here the wind

speed going into the underlying equations (4.6) and (4.7) is only the portion perpendicular to the rotor plane, denoted as $v_{rel,shft}$. It can be seen that using only the portion of the rotor effective wind speed perpendicular to the rotor plane for the calculation of thrust coefficients as has been done in figure 4.2 yields no variation for different yaw errors. As a consequence, it is a plausible

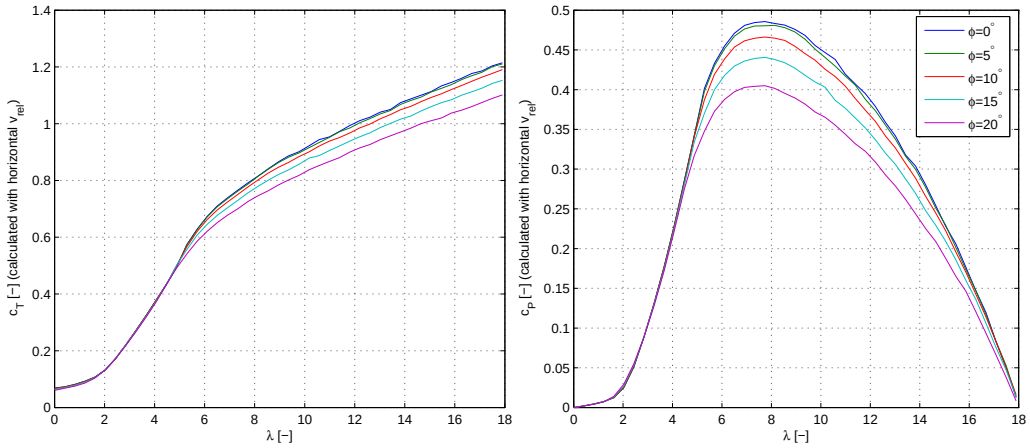

Figure 4.1: Power and thrust coefficients over tip-speed ratios λ for different yaw errors calculated with the horizontal portion of the rotor effective wind speed.

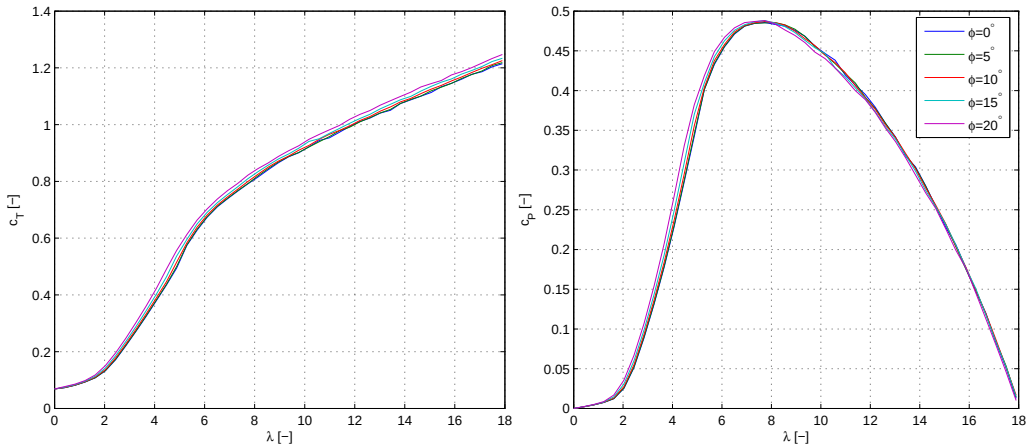

Figure 4.2: Power and thrust coefficients over tip-speed ratios λ for different yaw errors calculated with the portion of the rotor effective wind speed normal to the rotor plane.

method to approximate the effect of rotor alignment error using only the cosine portion of the wind speed to calculate the thrust force F_{aero} of the reduced model.

With this model for oblique inflow the magnitudes of forces and torques on the rotor hub with respect to the alignment error is given. However, another result of oblique inflow is that the thrust force does not apply exactly on the hub but eccentrically on the rotor plane. This is mostly observable when looking at the steady states of the overall FOWT plant with steady inflow. The arising restoring torque on the hub about y through the pitch misalignment yields a smaller platform pitch angle. This is how the effect was originally found and regarded as not negligible because of steady state deviation towards the reference model FAST. Figure 4.3 shows the location where the thrust force exerts on the rotor plane for various angles of misalignment in yaw and different tip-speed ratios λ. In the plot that is shown in *rotor*-coordinates it

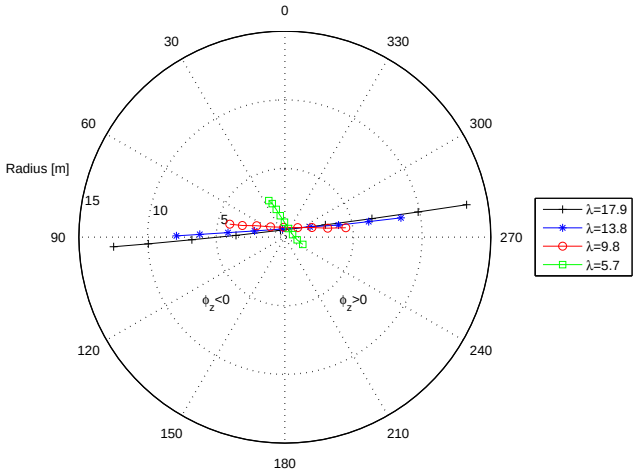

Figure 4.3: Location of thrust force exertion for yaw misalignment of $(-20° \dots 20°)$ and $\theta = 0°$.

can be seen that the lever arm of the thrust force with respect to the hub increases for higher tip-speed ratios in the same way as the resulting moment about the $rotor_3$-axis, $M_{Hub,z}$. Another observation is that the exertion location deviates from the horizontal axis in the direction of rotation, especially for small tip-speed ratios. This data is calculated with AeroDyn, see [1] that is integrated in FAST and based on BEM theory, see section 4.1. There exist various other models to predict the effect of oblique inflow. It is to mention, however, that the phenomenon is very complex and not easy to model. For a basic theoretic discussion of the effect, see Glauert's Momentum Theory in [20]. The data that is gained here is used to calculate the external aerodynamic torques on the rotor about both, the second and third *rotor*-axes. Although simulations have shown promising results for the load cases shown in chapter 6 the range of validity of the presented method has to be further analyzed.

With the power and thrust coefficients $c_P(\lambda, \theta)$ and $c_T(\lambda, \theta)$ and the location of thrust force exertion $\boldsymbol{r}_{F_{aero}}^{rotor}$ data tables are available to calculate the rotor kinetics in order to feed them into the multibody system. Besides an interpolation strategy an approximation of the three-dimensional functions is being tested at the moment. The reduced model code provides these different levels of disturbance reduction. Speed and accuracy benefit of the two methodologies also has to be further analyzed.

At this point all subsystems which had been first introduced in figure 1.1 are described so that the next chapter will deal with the programmatic implementation of the overall system.

Chapter 5

Reduced Model Simulation Code

The model derived up to this point is realized within the Matlab and Simulink environment. Therefore, the equations of motion of the multibody system are symbolically set up and integrated in a C-code S-Function together with the functions for the external forces. The set of ordinary differential equations is integrated in time through a fixed-step fourth-order Runge-Kutta method.

Before the calculation of the multibody system equations is done the user has to define a vector of degrees of freedom among the choice of the maximum number of 9 as described in chapter 2. Furthermore, the sequence of rotations can be selected, see section 2.1.1 and lastly there is an option to select whether equation (2.26) or equation (2.27) is given symbolically in C-code. The inversion of the mass matrix, see equation (2.28), is always done with numerical values applying a Cholesky decomposition, see [21]. The interface to all external forces from aerodynamics, hydrodynamics and also the mooring system is done through separate functions. These functions receive a position vector from the multibody system equations and return a vector of forces and moments about the specific reference point. The data exchange between the different function blocks is illustrated in figure 5.1.

Several flags allow a setting of the level of disturbance reduction. Line forces, for example, can be gained through an interpolation of the three-dimensional function with respect to horizontal and vertical displacements or based on the linearized stiffness parameters given in section 2.2. Hydrodynamic forces can be calculated based on the saved timeseries of wave height or, as is the methodology applied in most marine engineering codes, see section 3.2, based on a vector field of fluid particle velocities and accelerations over depth. Within the reduced model code it can also be calculated based on the wave height only through a simplification of linear wave theory through the method introduced in section 3.4. A capability to simulate sea currents based on the realization in FAST has been

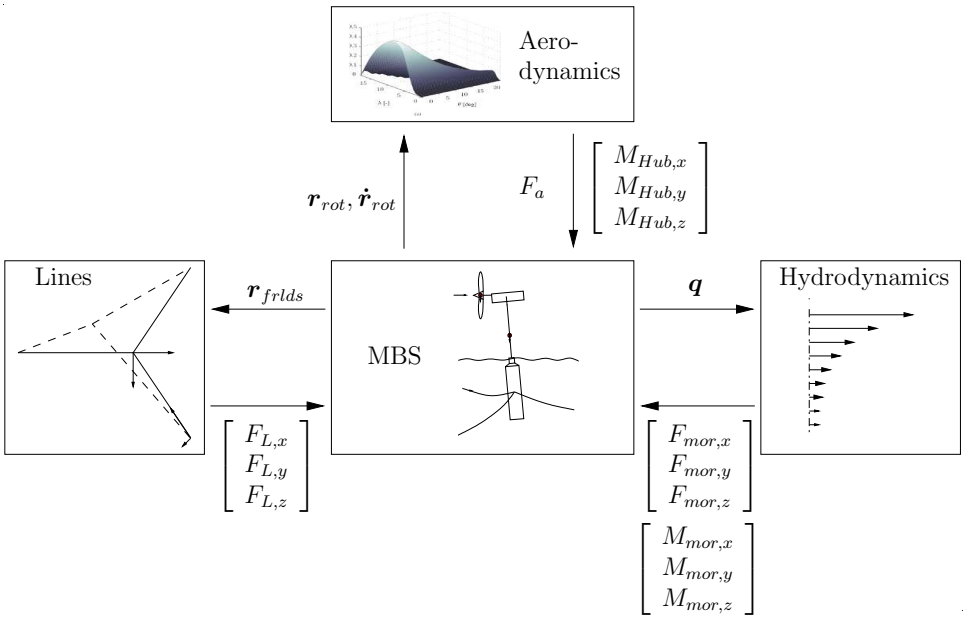

Figure 5.1: Interface between MBS and external force calculation modules.

implemented in the same way as the option for a misalignment of wind and waves. Aerodynamic forces are calculated based on an interpolation of dimensionless coefficients as described in chapter 4 or set to zero for simulations that assume no aerodynamic loads. A polynomial approximation of the three-dimensional curves of the coefficients will be realized in further model developments. Figure 5.2 illustrates the process of execution for a simulation generally with the lowest level of model reduction which means that all external forces are calculated through an interpolation of previously gained data. A further look is here taken at the hydrodynamic model and its simplification. The two paths show the difference of execution sequence when the reduced hydrodynamic model is applied instead of the original Morison Equation which requires the full wave kinematics as input.

A second order linear pitch actuator model is included in both, the Simulink-integrated FAST model and the reduced model, see [9] for a detailed description. The system is based on a PI-blade-pitch-to-feather controller and a standard variable-speed controller which are both implemented in Simulink block diagrams. The controller parameters are optimized for the FOWT as given in [2].

The programmatic realization has been optimized with respect to speed. In this process it turned out that the fastest option within Simulink is the integration of all functions in the C-code S-Function avoiding further Simulink blocks (graphical or as embedded functions) as part of feedback-loops. The finally achieved perfor-

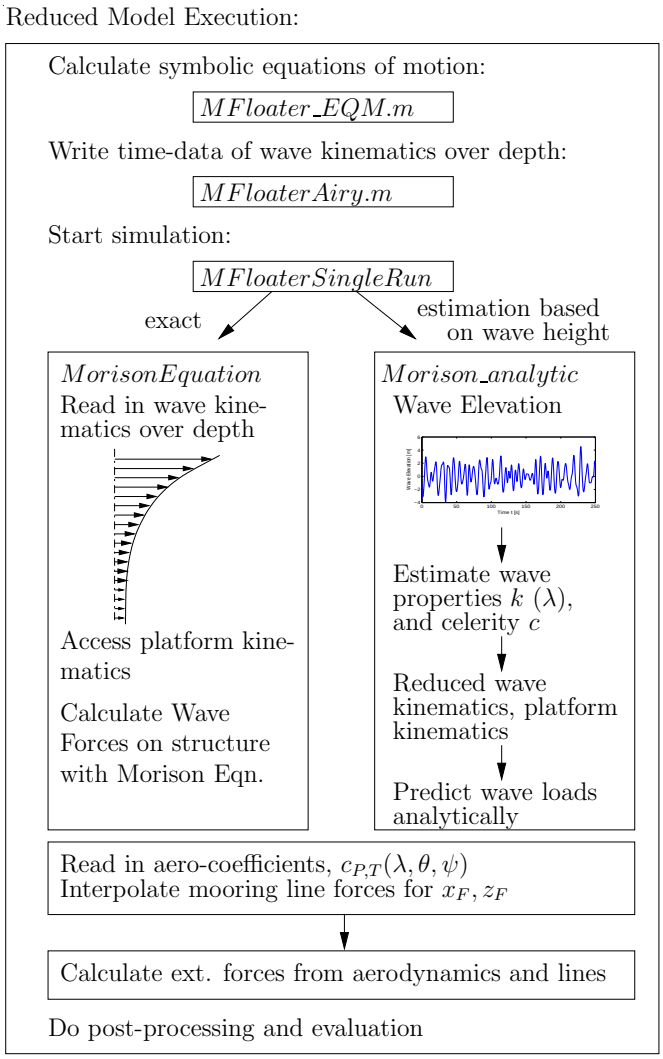

Figure 5.2: Execution procedure of reduced simulation code.

mance is a real-time factor of 100 meaning that a time-simulation of 10 minutes can be realized in 6 seconds. Finally, post-processing capabilities including an animation have been elaborated in order to make simulation results more ostensive. The next chapter will now give a detailed evaluation of all parts of the model through the simulation of several load cases by both, the reduced model code and the reference model FAST.

Chapter 6

Model Evaluation

The built simulation model for the floating offshore wind turbine is compared with the FAST aero-hydro-elastic model in order to evaluate its performance and validity. For the comparison various load cases that refer to the Offshore Code Comparison Collaboration (OC3), [16], are simulated and the most relevant shown in this chapter. The evaluated platform displacements are compared at SWL, see figure 2.2, in the inertial coordinate system with x pointing in wind direction as is the standard output of FAST. Tower top displacements are given in the local tower coordinate-system.

6.1 Platform step response

The step response of the platform, figure 6.1, mostly assesses the hydrodynamic model and the mooring system model. The platform is released from an initial pitch angle of $\psi_0 = 10°$ as in OC3 load case 1.4. There is no excitation from wind and waves so that $v_0 = 0$ and $\eta = 0$. With no wave loads the terms including wave velocity and acceleration of Morison's Equation (3.17) are of no impact. Thus, platform added-mass and the hydrodynamic damping as well as the hydrostatic restoring forces and moments are the ones to characterize the dynamics of this load case along with the line forces on the fairleads. Basic model characteristics are confirmed with this simulation as all steady states coincide with the FAST reference. Prevailing frequencies also match with the reference for all outputs, except for smaller oscillations in surge-direction. The rotational displacement about the y-axis shows a small mismatch in amplitude. This is most probably due to the different description of rotation used in the two models. Whereas the sequence of rotation is not specified in FAST it is stated that the sequence is of no importance for the expected small angles. The chosen rotation tensors in this model also aim at reducing this dependency, see

section 2.1.1. However, FAST uses a nonlinear but simplified description of rotation so that such misalignments in amplitudes of *PtfmPitch* might be assigned to this difference. The timeseries of the rotational displacement about x shows no obvious correlation in amplitudes and signs of displacements towards FAST. This is the case for all displacements in the non-excited directions for most performed simulations. These motions can be described as evasive, so that they are naturally small compared to directly excited degrees of freedom. The reason for the misalignment can be sought in the undetermined and minor excitation.

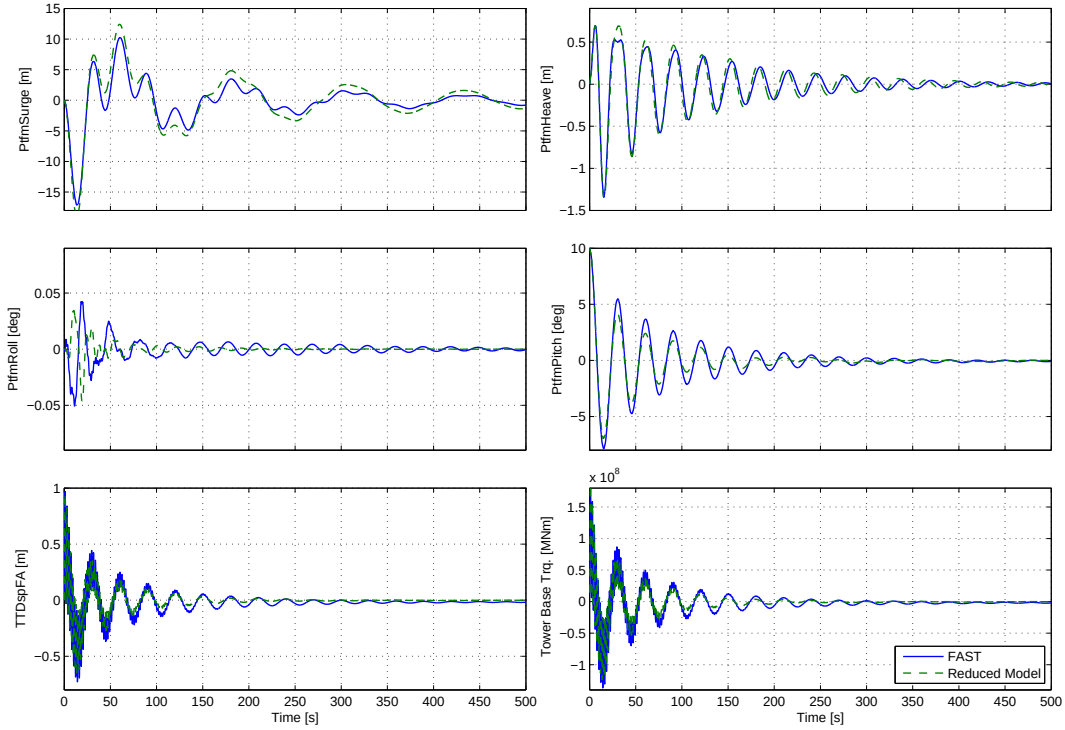

Figure 6.1: Free decay from platform pitch $\psi_0 = 10°$.

As the hydrodynamics in still water are mostly assessed in the last simulation the aerodynamics are now added with a wind excitation of $v_0 = 8\,\mathrm{m/s}$, see figure 6.2. The simulation is still a step-response but due to the now arising force on the rotor the platform is released from an initial upright position and displaced in wind direction. The displacement of the plant in wind direction proves the aerodynamic and mooring system model. The horizontal portion of the thrust force is completely compensated by the restoring mooring lines. The offline solution of the nonlinear system of equations (2.30) and (2.31) is interpolated in this simulation which leads to a good agreement in the steady state of *PtfmSurge*. The effects of a low-order approximation of the mooring functions will be assessed later in figure 2.4. The comparison of displacements in z-direction shows an

agreement in frequency but a small deviation in amplitudes. Since the frequency matches it is likely that a contribution from aerodynamics yields this difference. For the *PtfmRoll*-displacements the frequency and amplitudes matches now well with only a small mean offset. This might also be due to different rotation tensors. The *PtfmPitch* displacement as the inclination of the buoy and wind turbine due to the aerodynamic thrust force correlates well with FAST in frequency and steady state. The amplitude of this oscillation is a bit smaller for the reduced model in a comparable way as the *PtfmHeave*-displacement. A difference of damping in this direction is not likely since the frequencies coincide. Besides the mentioned cause in hydrodynamics a reason might be the different solution of the radiation problem which itself includes frequency-dependent damping in FAST whereas the reduced model assumes the damping coefficient to be constant. The tower top displacement is strongly related to the tower base moment shown at the bottom of figure 6.2. The correlation of steady states confirms the basic model agreement of the wind turbine. The small difference of the steady state in tower top displacement can be assigned to the fact that the pre-cone angle of the blades is neglected in the reduced model. This initial inclination of the blades in wind direction leads to a torque on the rotor hub about y as long as the blades are not bent back to the hub-level. This thrust force-dependent effect is considered negligible within the objectives of the reduced model.

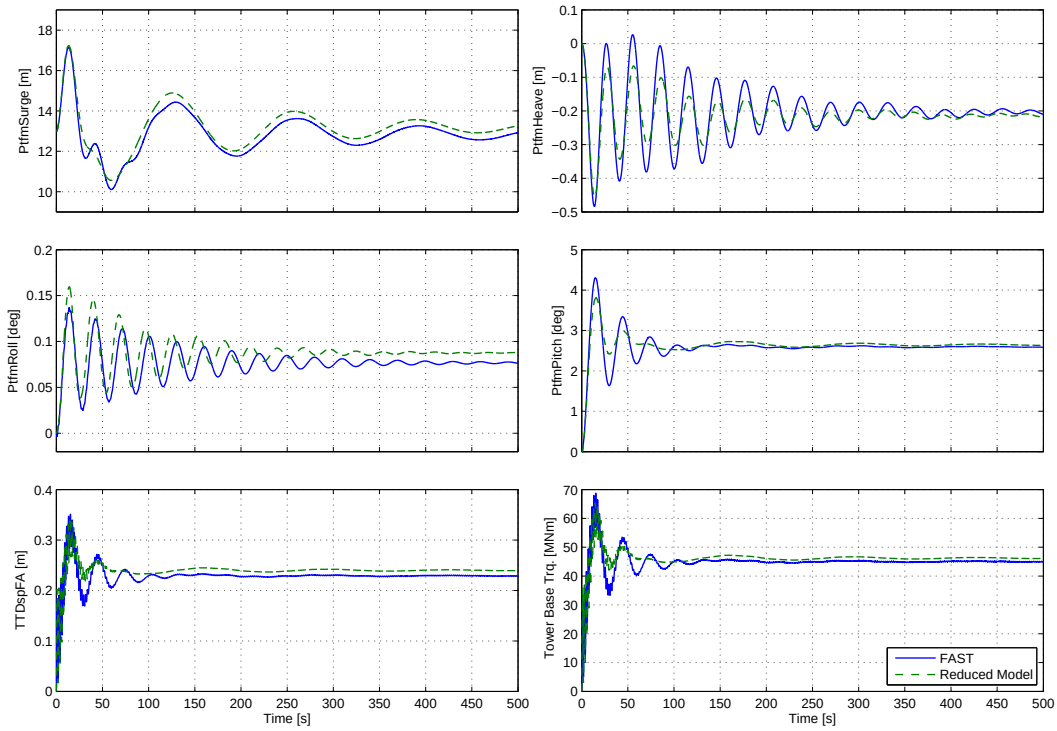

Figure 6.2: Free decay from upright pos., $v_0 = 8\,\mathrm{m/s}$.

With the step-response a meaningful load case for the hydrodynamic model is simulated. So far, no wave loads have been applied on the system and external forces from hydrodynamics and aerodynamics are not stochastic as they would realistically be. In the next section turbulent wind will excite the rotor with a combination of still water, regular and stochastic waves.

6.2 Stochastic wind, coupled with still, regular and stochastic waves

With turbulent inflow another disturbance reduction is introduced to the assessment. The three-dimensional turbulent windfield is reduced to a one-dimensional hub-height timeseries according to [9], see chapter 4. The result of this estimation can be seen in v_0 on top of each figure on the left, next to the timeseries of the wave elevation η. In the next section all presented simulations are done with the full hydrodynamic model which means that Morison's equation (3.17) is integrated numerically using the offline-calculated wave kinematics over time. The FAST reference model has all degrees of freedom enabled, including first and second tower and blade modes so that it consists of 22 degrees of freedom in total.

6.2.1 Full hydrodynamic model

The first load case in this section assesses the hydrodynamic radiation problem. The floating structure is externally excited by the stochastic wind force whereas there is no wave action. Figure 6.3 shows the same plant displacements as the previous figure 6.2. In this load case the mooring model is also assessed. Besides a linear interpolation of the 50×50 grid in a range of 70 m in x- and 30 m in z-direction the linearized approach by [2] is evaluated. This linear model uses constant stiffness factors that represent the line properties in all horizontal and vertical directions. The linearization is based on the initial platform position. The agreement of the linear model is still mostly valid for a displacement of $10 \ldots 15$ m in surge-direction. A deviation occurs for the heave-displacement when the *PtfmSurge*-displacement exceeds 15 m. The overall agreement confirms the statement by [2] that the memory effect, inherent in the radiation problem, is negligible for the spar-buoy. The previously discussed amplitude of prevalent oscillations coincides well for the pitch angle but is slightly too small for the surge-displacement. Also the *PtfmRoll*-excitation seems to be bigger for the reference model. This might be ascribed, again, to the different approach of the hydrodynamic modelling. The evasive excitation in y-direction might also be due to the turbulent rotor-excitation and the therewith involved force application in

side-side direction. The structural dynamic response of the flexible blades is not considered which was part of the objectives of this model. The high-frequency aerodynamic excitation, however, is lost when reducing the vectorial wind field to a scalar one. The exact interdependence of blade flexibility and the wind turbulence will have to be further analyzed. The therewith occurring high-frequency oscillations are not important for a collective pitch control with NMPC but potentially for the fast load case simulations that assess also tower base moments where high frequency stresses might be of importance.

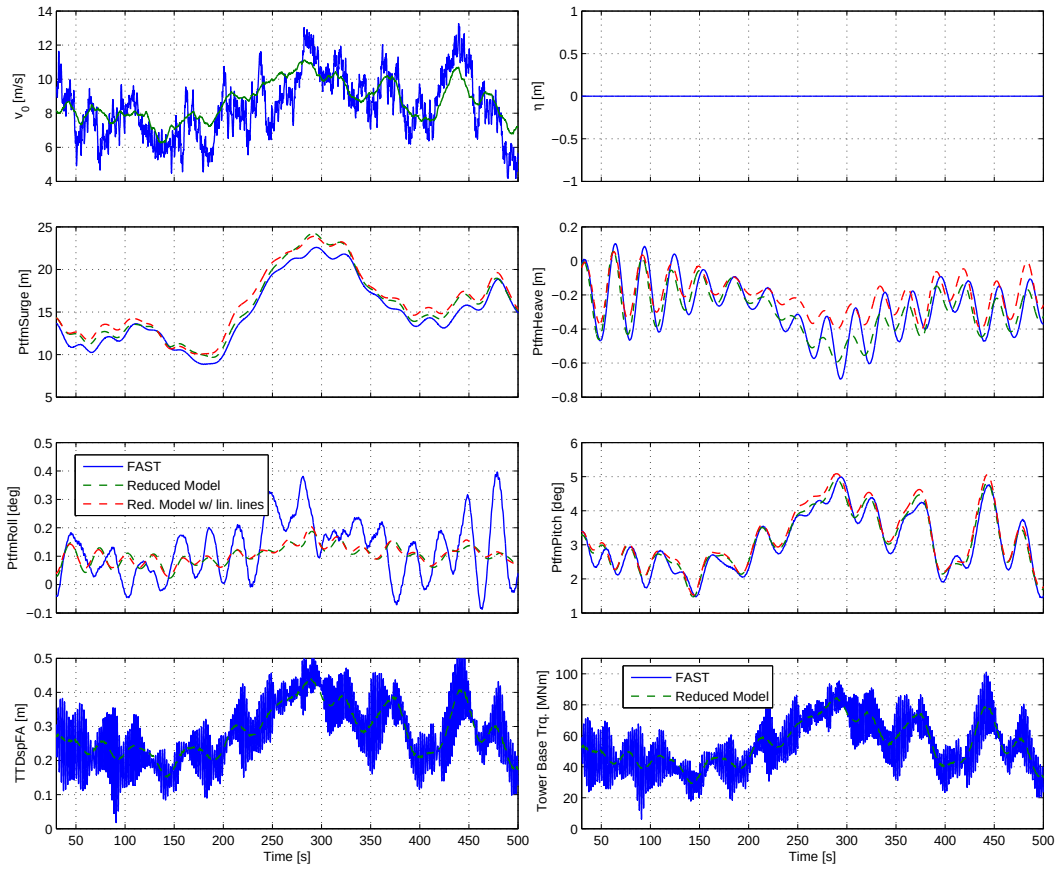

Figure 6.3: Stochastic wind (turb. class A, $v_0 = 8\,\mathrm{m/s}$), still water.

The comparison depicted in figure 6.4 extends the previous analysis of figure 6.3 so that the dependency of aerodynamic forces on the blade pitch angle is assessed. The chosen mean wind speed of 20 m/s lies above rated wind speed and therefore yields action of the pitch actuator. The signals of the blade pitch angle and the angular rotor speed are shown below the inputs on the second line. A high-frequency motion of the pitch actuator seems to yield deviating dynamics of the platform. This effect can be ascribed to the high non-linearity

of the pitch-controller and the underlying aerodynamic model. It is stated again, however, that both, torque and blade pitch controllers are the standard baseline controllers for both models. The tower top displacement coincides well in the range of the platform frequencies but damps out higher frequencies in the case of the reduced model as discussed before.

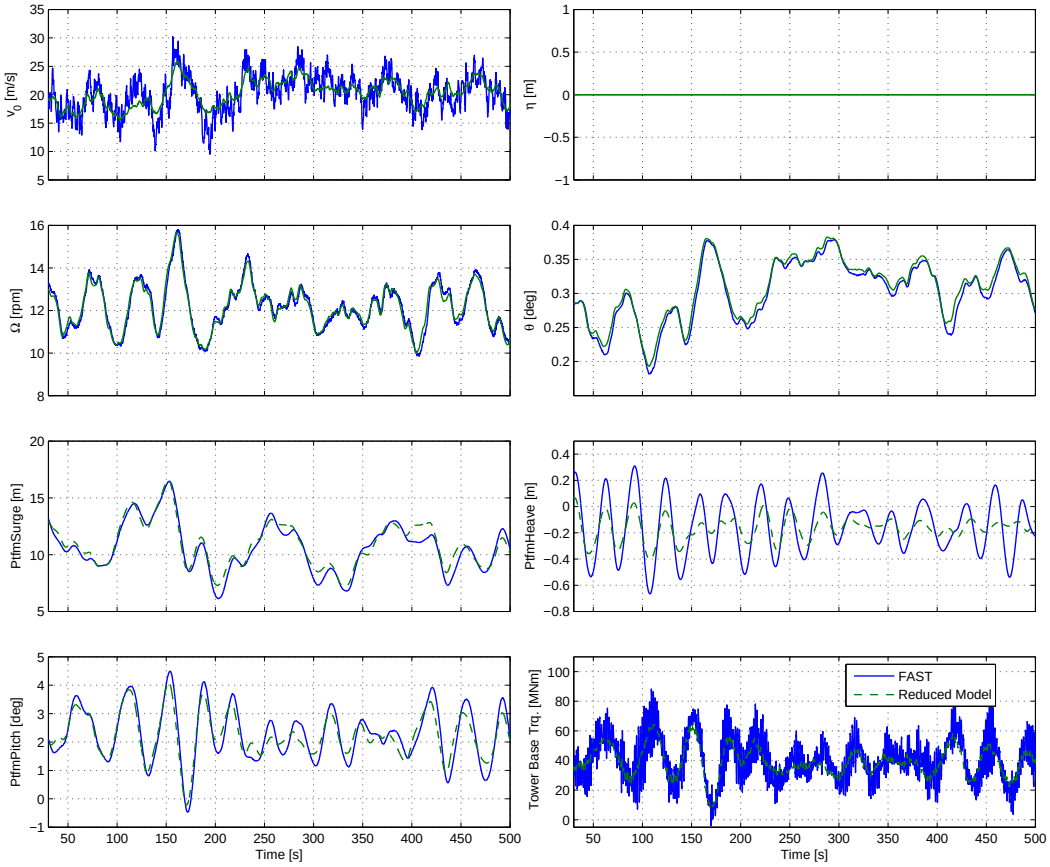

Figure 6.4: Stochastic wind (turb. class A, $v_0 = 20\,\mathrm{m/s}$), still water.

The last comparison of figure 6.4 is now taken as a reference when regular waves of $T_p = 10\,\mathrm{s}$ and $H_s = 6\,\mathrm{m}$ are added, see figure 6.5. The platform displacements in x-direction and about y behave comparably to the previous load case and therefore confirm the full wave model for this regular wave. The *PtfmHeave*-displacement, however, is mostly phase-lagged towards the reference by 180°. This phenomenon will have to be further analyzed in future work. Whereas the plant oscillates in heave-direction in phase with the waves for the reference model, it only switches to the in-phase oscillation for $T_p > 30\,\mathrm{s}$ in the case of the reduced model. The forces in z-direction on the platform arise only from the hydrostatic pressure-integration over depth, see equation (3.4) in this model. A simple harmonic oscillator with the same mass data as the FOWT model and

the same stiffness and damping parameters has shown the same behavior as the reduced model which attests the correctness of the modelling. Dynamic forces that are not appearing in the reduced model but in the reference model might originate from frequency-dependent wave excitation on the platform and yield the discussed deviation in heave direction.

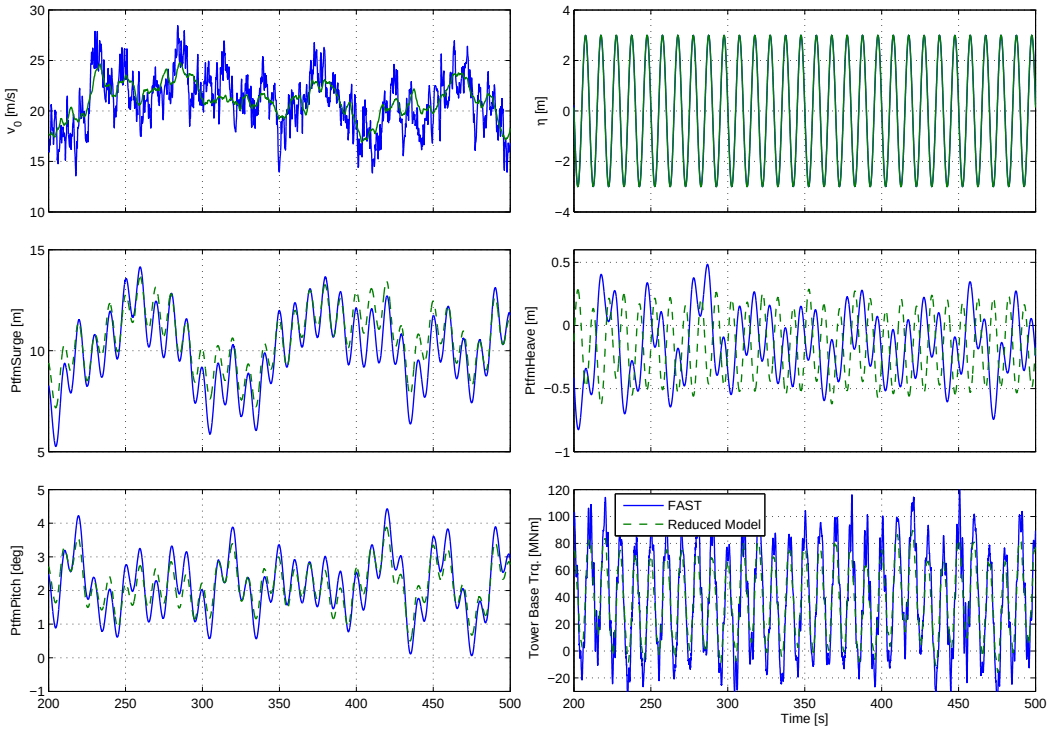

Figure 6.5: Stochastic wind (turb. class A, $v_0 = 20\,\mathrm{m/s}$), regular waves.

The next simulated load case shown in figure 6.6, comparable to IEC 5.2, is turbulent wind with a mean of $v_0 = 8\,\mathrm{m/s}$ and irregular waves as given in the Pierson-Moskowitz-Spectrum, see figure 3.3, with a peak spectral period $T_p = 10\,\mathrm{s}$ and a significant wave height of $H_s = 6\,\mathrm{m}$. The comparison with FAST is realized through the power spectral densities of the degrees of freedom *PtfmPitch*, *PtfmSurge* and the tower base moment M_{yT}. Results are only shown in frequency domain since the reduced model applies the full hydrodynamic model (original Morison Equation) so that the whole timeseries of fluid particle-kinematics over depth is needed as input. Thus, only frequency characteristics of the disturbances coincide in the two models in this load case. The two peaks of the wave excitation frequency and the tower eigenfrequency are observable. Although the reduced model shows a higher energy content for the second frequency peak the frequencies of the peaks coincide very well which backs the wave-structure model as well as the aerodynamic model. This load case is already a most realistic one since both disturbances from wind and waves are stochastic and in a range that yields

pitching of the rotor blades. In a next step the reduced hydrodynamic model is assessed.

6.2.2 Reduced hydrodynamic model

In this section the reduced hydrodynamic model, presented in section 3.4.1, is evaluated. The model estimates wave loads based on the wave elevation η, only and approximates wave kinematics over depth through an exponential function so that the integration of Morison's Equation (3.17) does not have to be done numerically. Figure 6.7 shows the same load case as the previous one but includes now time-domain graphs since the wave elevation is adopted from FAST. The overall behaviour of the platform displacements and the tower base moment is well aligned with FAST. Also the power spectral density plots the angular rotor speed and the tower base moment is very promising in the range of low frequencies below 0.4 Hz as was the objective for the reduced model. Besides the out-of-phase motion of the platform in z-direction the *PtfmSurge*- and *PtfmPitch*-motions deviate further from the reference in longer wave periods as in the previous simulation. A reason for this is most probably the approximation of wave kinematics according to the peak spectral period so that waves with a smaller frequency will

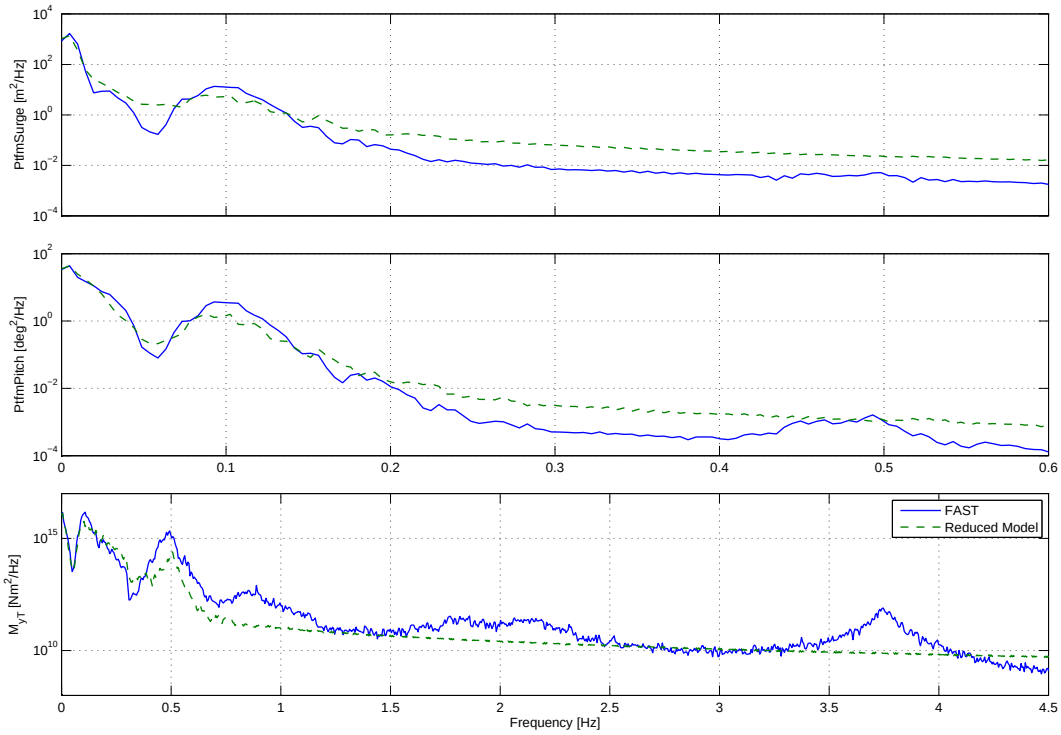

Figure 6.6: Turbulent wind (turb. class A, $v_0 = 8\,\mathrm{m/s}$), irregular waves.

not be represented to the full extent. The dependency of the approximation on the wavelength is discussed in section 3.4.1.

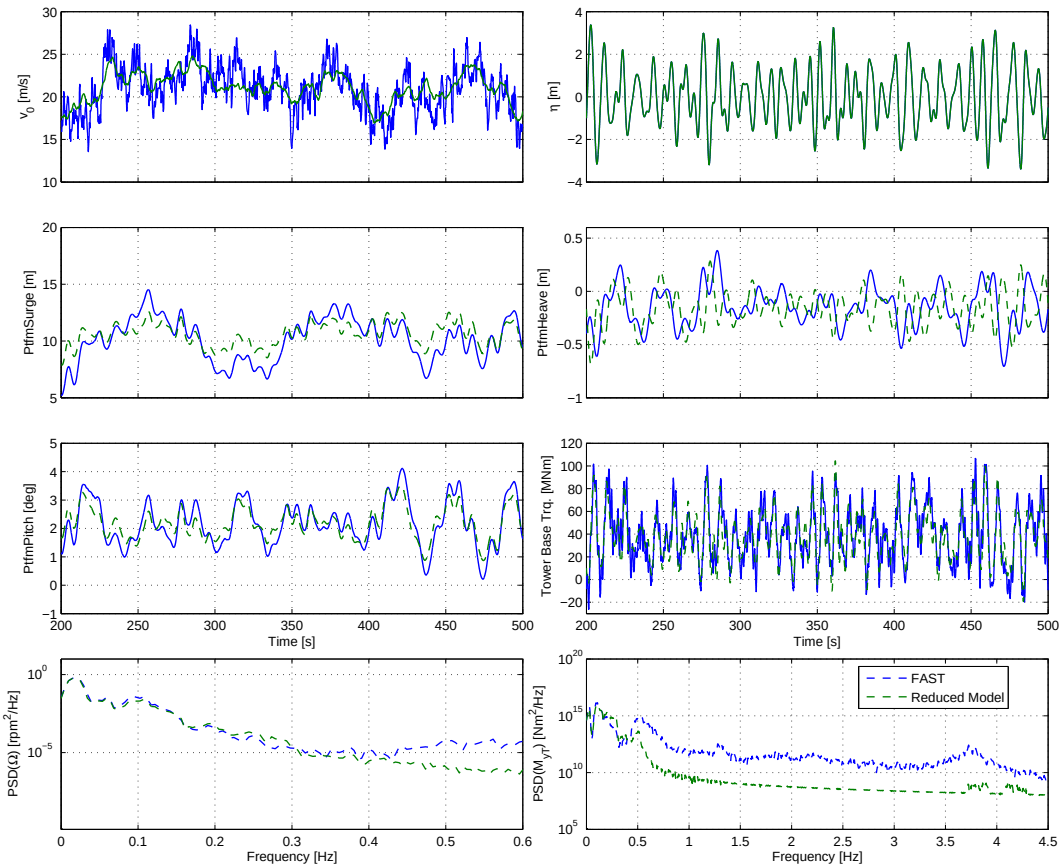

Figure 6.7: Turbulent wind (turb. class A, $v_0 = 20\,\mathrm{m/s}$), irregular waves, reduced hydrodynamics.

Eventually, it is concluded that first, steady states of the FOWT model match with the reference model very well, second, the low-frequency excitation from waves up to the resonance of the tower bending is well represented in the reduced model which was the initial target for this project. In the next chapter a concluding summary of the project is given with several indications for future work.

Chapter 7

Conclusion and Outlook

The purpose of this work was to elaborate a reduced numerical model for the spar-buoy floating offshore wind turbine concept that reliably represents the overall nonlinear low-frequency behaviour. Complex inputs into the system like vector fields of wind and fluid velocities should be avoided and a reduction to measurable quantities was sought. In order to pursue this goal a multibody system consisting of four rigid bodies with nine degrees of freedom according to the Newton-Euler formalism has been set up. Except for the tower no body elasticities have been considered and the blades comprised in a single body for the whole rotor disk. The symbolic equations of motions are integrated in a compilable code allowing a high computational speed.
Disturbances coming from wave loads are modeled in time-domain avoiding large geometry- and frequency-dependent vectorial quantities. One realization is a conventional application of Morison's equation that returns forces on finite sections of the buoy with respect to relative undisturbed fluid particle kinematics. In a next step this implementation was sought to be simplified in order to reduce the disturbance input from vectorial velocity and acceleration timeseries to a single wave elevation. This estimate also avoids a numerical integration over foresaid platform sections. The approximation is based on a prevailing wavenumber according to a given wave spectrum or on an online update of wave frequency information within the reduced hydrodynamic module.
Aerodynamic disturbances have been modelled based on an estimate of a scalar wind speed at hub height out of the three-dimensional turbulent inflow. Furthermore, the effect of oblique inflow which is more likely to occur with floating plants than their onshore counterparts is accounted for. The disturbance models have been developed for a future use within Nonlinear Model Predictive Control of the FOWT. The high real-time factor of 100 also motivates for an application in extensive load case simulations during the design phase of new concepts. These load cases that are, e.g., specified by the IEC are numerous and

the high computational effort demonstrates a significant obstacle for the design of new FOWT concepts. The validity of the model for low frequencies and major internal forces has been proved by a comparison with the certified FAST model. The compared load cases have been chosen in order to assess the structural model as well as the disturbance models as independently as possible. The results agree very well in the initially set frequency range of importance and are promising for future development and application of the reduced model.

Future work on this project should aim at further improvement of the model in terms of computational efficiency and speed. Additional levels of model and disturbance reduction can be implemented. An improved algebraic approximation of line forces and aerodynamic coefficients will have to be implemented and tested. For the final integration of the reduced model into the NMPC a real-time estimate of the peak spectral wave frequency as well as the wave propagation direction needs to be found. The presented aerodynamic model offers further potential of improvement, especially for the application with FOWTs. The effects of wind shear, for example, are neglected so far. These effects are then important when considering individual blade pitch control (IPC). It is possible to optimize the WT performance by including individual bodies for each blade in the reduced multibody model and extent NMPC for IPC. The use of the reduced model for conceptual design will require an alternative formulation of the hydrodynamic equations. So far, only slender cylindrical structures can be analyzed due to the implementation of Morison's equation. All extensions, however, will need to be simple and computationally efficient in order not to loose the computational speed of the model, which is the special advantage to most state-of-the-art tools.

Appendix

A.1 Turbine Geometry Data

The complete set of the OC3-Hywind FOWT model data can be found in [2]. The numerical values and a sketch of the geometry of the model implemented in the reduced code can be found in Figure A.1.

A.2 Content of CD-ROM

The attached CD-ROM contains the following elements on top level

- **DIPL_187.pdf**: PDF-File DIPL–187.
- **DIPL_187/**: a directory with TEX-files of the report DIPL-187 as well as all included graphics as *.eps and *.svg files.
- **DATA/**: a directory with all necessary data, tools, scripts and programs.

Additional information is available in readme.txt-files in the according directories.

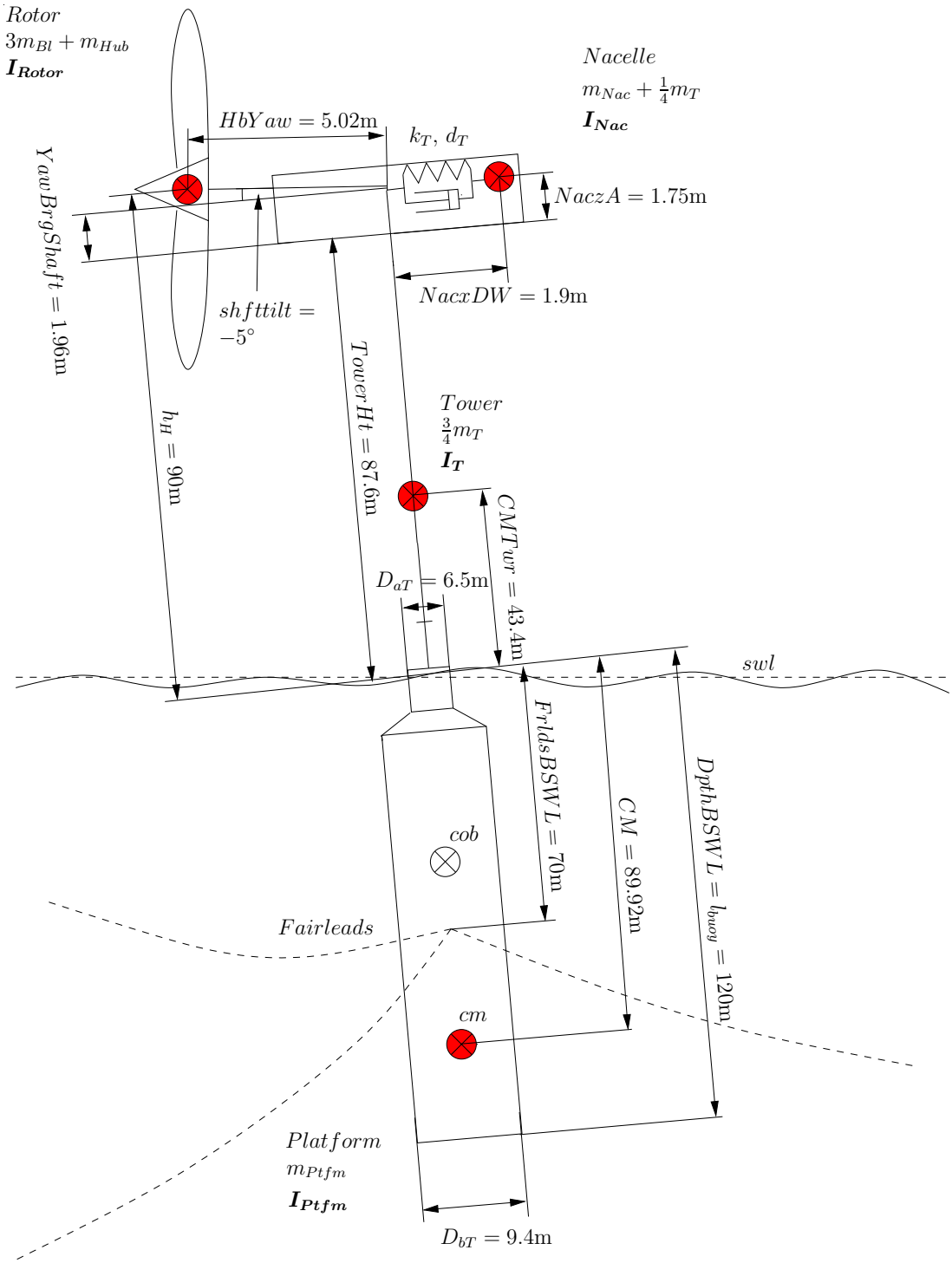

Figure A.1: OC3 Hywind FOWT model - geometry data.

Bibliography

[1] Jonkman, J.; Buhl, M.L.: Fast User's Guide. NREL, 2005.

[2] Jonkman, J.: Definition of the Floating System for Phase IV of OC3. Tech. rep., NREL, Golden, CO/USA, 2010.

[3] Nitsch, J.: Die Bedeutung erneuerbarer Energien in der zukünftigen Energieversorgung. In Bremer Forum für Wissenschaftsjournalismus, DLR-Institut für Technische Thermodynamik, Abt. Systemanalyse und Technikbewertung, 2005.

[4] Ender, C.: Wind Energy Use in Germany - Status 31.12.2011. DEWI Magazin, 2012.

[5] Krohn, S.; Morthorst, P.E.; Awerbuch, S.: The Economics of Wind Energy. Tech. rep., The European Wind Energy Association (EWEA), 2009.

[6] Wilkes, J.: The European Offshore Wind Industry Key 2011 Trends and Statistics. Tech. rep., European Wind Energy Association (EWEA), 2012.

[7] Wayman, E.: Coupled Dynamics and Economic Analysis of Floating Wind Turbine Systems. Master's thesis, Massachussetts Institute of Technology, 2006.

[8] Karimirad, M.; Moan, T.: A Simplified Method for Coupled Analysis of Floating Offshore Wind Turbines. Journal of Marine Structures, 2012.

[9] Schlipf, D.; Schlipf, D.J.; Kühn, M.: Nonlinear Model Predictive Control of Wind Turbines Using LIDAR. Wind Energy, 2012.

[10] Matha, D.; Sandner, F.; Schlipf, D.: Efficient critical design load case identification for floating offshore wind turbines with a reduced nonlinear model. In The science of making torque from wind, 2012.

[11] Schiehlen, W.; Eberhard, P.: Technische Dynamik - Modelle für Regelung und Simulation. Stuttgart: B.G. Teubner, 2012.

[12] Jonkman, J.: Dynamics Modeling and Loads Analysis of an Offshore Floating Wind Turbine. Ph.D. thesis, National Renewable Energy Laboratory, 2007.

[13] Gasch, R.; Twele, J.: Windkraftanlagen - Grundlagen, Entwurf, Planung und Betrieb. Wiesbaden: B.G. Teubner, 2005.

[14] Massachussetts Institute of Technology: Wamit User Manual, version 7.0. Edn.

[15] McCormick, M.E.: Ocean Engineering Mechanics. Oxford University Press, 2010.

[16] Jonkman, J.; Musial, W.: Offshore Code Comparison Collaboration (OC3) for IEA Task 23 Offshore Wind Technology and Development. Tech. rep., NREL, Golden, CO/USA, 2010.

[17] Östergaard, C.; Schellin, T.: Comparison of Experimental and Theoretical Wave Actions on Floating and Compliant Offshore Structures. Applied Ocean Research, Vol. 9, No. 4, 1987.

[18] Jonkman, B.; Kilcher, L.: TurbSim Users's Guide. NREL, 1.06.00. Edn., 2012.

[19] Schlipf, D.; Kapp, S.; Anger, J.; Bischoff, O.; Hofsäß, M.; Rettenmeier, A.; Kühn, M.: Prospects of Optimization of Energy Production by LIDAR Assisted Control of Wind Turbines.

[20] Burton, T.; Jenkins, N.; Sharpe, D.; Bossanyi, E.: Wind Energy Handbook. Wiley, 2nd. Edn., 2011.

[21] Press, H.; Teukolsky, S.; Vetterling, W.; Flannery, B.: Numerical Recipes 3rd Edition: The Art of Scientific Computing. Cambridge University Press, 2007.